integrity Research Journals

Applied Journal of Physical Science
Volume 3(2), pages 37-60, April 2021
Article Number: EA9433402
ISSN: 2756-6684
https://doi.org/10.31248/AJPS2021.045
https://integrityresjournals.org/journal/AJPS

Full Length Research

Series of 1-D ER and IP traverses reveal vestige of regional geological structure

Jonah, S. A.

Department of Physics, Federal University of Technology, Minna, Nigeria.

Email: sajonah2003@yahoo.com

Received 4th April, 2021; Accepted 29th April, 2021

ABSTRACT: At the Basement Complex geological province of central Nigeria, in the state of Niger, just northeast of the Bida Sedimentary Basin, there is the character of non-complexity and high uniformity in the local geology over an appreciable linear spread. This appreciation makes it a standard practice to do one-dimensional vertical electrical sounding surveys in the search for groundwater resources at this area with the expectation of reliable results. This seeming "simplicity" means that intense manual labour can be invested in acquiring a large data-field at a local area of survey where resources are not readily available to do a standard two-dimensional survey of the conventional kind. This is especially significant for the proposed area of development at the Gidan Kwano Campus of the Federal University of Technology, Minna, Thus, with this awareness and the use of the ABEM Terrameter 4000 equipment, the aim of this study was to do an intense acquisition of one-dimensional electrical resistance and concomitant induced polarization programme for this proposed area of development so as to achieve the objective of garnering information about exploitable groundwater locations before structural developments cover these points up. Typical point-to-point one-dimensional tandem electrical resistance and concomitant induced polarisation surveys were completed along east-west profile lines for about 309 survey stations of the available 441 principal locations of the 4 km^2 extent of the proposed new development. After due processing and interpretation of the data-field of this survey, whilst remarking that the induced polarisation data-set was used herein as quality control "refiner" only, clusters of reliable groundwater locations were observed at the southwest end of the 4 km^2 areal extent of the proposed new development. It conforms to the dip of the landform and comparatively significant overburden-material thicknesses observed over there. Interestingly, in a twist of serendipity, the series of diagonal subsurface "fault-lines" that connect one promising groundwater prospect with the other, describable by a prominent northeast-southwest dip, aligns exactly with the Kazaure-Karaukarau-Kushaka-Ilesha Schist Belt. In the modern geography setting of the present time, the Kazaure-Karaukarau-Kushaka-Ilesha Schist Belt actually traverses a lengthy diagonal across the landscape of Nigeria, cutting through such Nigerian states as Jigawa, Kano, Kaduna, Niger, Kwara, Ekiti, and Osun. There is virtually no surface indicator of this once-prominent schist belt and what this study reveals is its vestigial signature.

Keywords: ER, fault-traces, groundwater, homogeneity, IP, one-dimensional, schist, vestige.

INTRODUCTION

At a 4 km^2 tranche of a 100 km^2 swath landmass that is the Gidan Kwano Campus (GKC) of the Federal University of Technology (FUT), Minna, Nigeria, a series of point-to-point electrical resistivity (ER) and induced polarisation (IP) surveys were completed along east-west profile lines for a 2 km^2 x 2 km^2 areal spread. These rather labourous tasks of 21 sequences of measurements for ER standalone (the configuration employed here was of the vertical electrical sounding or VES mode) and IP standalone at 100 m station-spacing were targeted towards the search for groundwater resources at the 4 km^2 tranche; this areal extent has been appropriately designated "Phase II Development" in the overall short- to mid-term plans of the FUT Minna. The desire was to

identify groundwater locations before structural developments cover these points up. Sustained groundwater yield has been a vexing problem at the developed portion of the GKC (the less than 2 km^2 "Phase I Development") for a long time now, and this situation is exacerbated by non-existent potable water supply to this university's campus from the state government's public utilities waterworks facilities located some twenty kilometers to the northeast. Thus, the idea of the cost-intensive series of one-dimensional (1-D) surveys was to "manually-discretised," if you will, acres of contiguous landmass in order "not to miss out" on potential groundwater prospects in the local basement geological province that is the area of study.

Literature review

Jonah and Adegboye (2019) wondered how much of the fact of the local geology guides the design and interpretation of the suite of geophysical surveys that are carried out at the wider area of which the tranche for this study is but a part. One of the areas of contention has been the insistence of carrying out two-dimensional (2-D) and three-dimensional (3-D) surveys and interpretation where just one-dimensional (1-D) field layout would suffice. The authors observed that, "Loke (2001) stated that it is assumed that the subsurface is 2-D when interpreting data from a single line; however, this assumption is valid if the survey is carried out across the strike of an elongated structure. Loke (2001) also pointed out that, if there are significant variations in the subsurface resistivity in a direction perpendicular to the survey line, then the geology is 3-D. It is generally accepted amongst geoscientists of Nigeria that the local geology at a tranche of the Nigerian Basement Complex (NBC) does not differ appreciably over a wide area; this prevailing mindset was the basis of the 'robust inversion' protocol that Loke (2011) made regarding the production of 2-D inversion models for the data of the Wenner-Gamma array survey that Acworth (1981) reported for the Bauchi area of Nigeria even though the data for that Acworth (1981) survey was acquired many years before 2-D inversion software and fast micro-computers were widely available (basically acquired in the 1-D format). Thus, now, if there are no significant variations in the subsurface resistivity values along the direction of survey then this result further validates the generally accepted point-of-view that is held amongst geoscientists of Nigeria regarding the nature of the local geology at a province of the NBC. If physical properties of the materials in this geological province (resistivity, seismic velocities, etc.) do not change much over a lateral extent then the case is now made for the justification of sticking to 1-D field layout, thus saving cost incurred in the course of surveys". Jonah and Adegboye (2019) concluded that a final median of median of medians of 53.08% for the correlation sequences of the available VES data-set for their study essentially translates to mean that there is high homogeneity in geological material distribution across the 2 km x 2km extent of the southern Phase II Development. This conclusion is significant in its implication for the requirement of necessarily doing a strictly 2-D survey at the area and its wider local basement province. Thus, now, series of 1-D survey procedures acquired along a profile can now be handled with 2-D processing software tools even if the survey is not carried out across the strike of an elongated structure. This is very significant in the quest to reduce cost incurred during VES surveys.

Loke (2001) stated that the purpose of electrical surveys is to determine the subsurface resistivity distribution by making measurements on the ground surface. The ground resistivity is related to various geological parameters such as the mineral and fluid content, porosity, and degree of water saturation in the rock. Electrical resistivity surveys have been used for many decades in hydrogeological, mining, and geotechnical investigations; its recent application is its use in environmental surveys. The author stated further that the fundamental physical law used in resistivity surveys is Ohm's law that governs the flow of current in the ground. The equation for Ohm's law in vector form for current flow in a continuous medium is given by:

$$J = \sigma E \quad (1)$$

where σ is the conductivity of the medium, J is the current density and E is the electric field intensity. In practice, what is measured is the electric field potential. The author pointed out also that in geophysical surveys the medium resistivity, ρ, which is equals to the reciprocal of the conductivity (ρ=1/σ), is more commonly used. The relationship between the electric potential and the field intensity is given by:

$$E = -\nabla\Phi \quad (2)$$

Combining Eqs 1 and 2, we get

$$J = -\sigma\nabla\Phi \quad (3)$$

In almost all surveys, the current sources are in the form of point sources. In this case, over an elemental volume ΔV surrounding the current source I, located at (x_s, y_s, z_s) the relationship between the current density and the current (Dey and Morrison, 1979) is given by:

$$\nabla.\mathbf{J} = \frac{I}{\Delta V}\delta(x - x_s)\delta(y - y_s)\delta(z - z_s) \quad (4)$$

where δ is the Dirac delta function. Eq. 4 can then be rewritten as

$$-\nabla\bullet[\sigma(x, y, z)\nabla\varphi(x, y, z)] = \frac{I}{\Delta V}\delta(x - x_s)\delta(y - y_s)\delta(z - z_s) \quad (5)$$

This is the basic equation that gives the potential distribution in the ground due to a point current source. A

large number of techniques have been developed to solve this equation. This is the “forward” modeling problem, that is, to determine the potential that would be observed over a given subsurface structure. Fully analytical methods have been used for simple cases, such as a sphere in a homogenous medium or a vertical fault between two areas each with a constant resistivity. For an arbitrary resistivity distribution, numerical techniques are more commonly used. For the 1-D case, where the subsurface is restricted to a number of horizontal layers, the linear filter method is commonly used (Koefoed, 1979). For 2-D and three-dimensional (3-D) cases, the finite-difference and finite-element methods are the most versatile. Akca (2016) posited that Mufti (1976), Dey and Morrison (1979a; 1979b) discussed the finite-difference approach whilst Coggon (1971), Rijo (1977) and Pelton et al. (1978) discussed the finite-element approach.

The IP method is closely related to the resistivity method, but the method requires significantly higher currents. IP surveys are able to detect conductive minerals of very low concentrations that might otherwise be missed by resistivity or electromagnetic (EM) surveys (Loke, 2001). According to this author, one of the distinctive characteristics of the IP method has been the different parameters in the time and frequency domains used to represent the IP effect. The IP effect is caused by two main mechanisms, the membrane polarisation and the electrode polarization effects. The membrane polarisation effect is largely caused by clay minerals present in the rock or sediment. This is particularly relevant in engineering and environmental surveys. The electrode polarisation effect is caused by conductive minerals in rocks such that the current flow is partly electrolytic (through groundwater) and partly electronic (through the conductive mineral). This effect is of particular interest in surveys for metallic minerals, such as disseminated sulfides. IP measurements are made in the time-domain or frequency domain. The time domain IP unit, the chargeability, is usually given in millivolt per volt (mV/V) or in milliseconds.

METHODOLOGY

Location of the study area

The 4 km^2 tranche lies between latitude $9^0$30′57.80″N;$9^0$32′02.58″N and longitude $6^0$25′39.00″E; $6^0$26′43.80″E. The grid of this 4 km^2 tranche at 100 m station-spacing is shown as Figure 1. The Gidan Kwano Campus, located along the Minna-Kateregi-Bida Road, lies between latitude $9^0$26′15″N; $9^0$37′30″N and longitude $6^0$23′15″E; $6^0$28′45″E (Adesoye, 1986); see Figure 2. Of particular interest about the Gidan Kwano Campus is its horse-shoe shape, as can be made out in Figure 2. As seen in Figure 2, and as pointed out in Adesoye (1986), Minna is located to the northeast of the Gidan Kwano Campus; the Gidan Kwano Campus is bounded to the north by the western railway line to Lagos, the Maikunkele railway station 11 km away, and the Minna-Tegina Road to the northwest. To the northeast are the Shadna Hill, the Minna International Airport and the Maikunkele Hill. To the entire east is the Minna-Bida Road bordering the site for 12 km; this starts from the Minna end at Km 74 and moves out of the road at Km 62. There are villages across this road for the entire 12 km stretch; some of these villages are Gidan Kwano, Dan Zaria, Gidan Panti, and Garatu. The Garatu Hill borders the site at the end of the southeast sector. The Dagga Hill and the Dagga River are found at the southwest sector of the site. To the northwest of the Gidan Kwano Campus is the Kpaina Hill straddling the GKC and the campus’ environ. The twin high tension electricity lines running from the northwest to the northeast, from Kainji to Shiroro passes within 5 km of the GKC.

Geology of the area of study

The area of study is underlain by Basement Complex rocks consisting of medium-grained biotite granite interbanded with coarse-grained leucocratic granite and intruded in places by quartzo-feldspar pegmatite dykes. The dykes strike parallel to the strike of the foliation, and they range from 0.5 to 3.5 m in diameter. Outcrops are found along the river valleys as flat-lying bodies. They range in sizes from 3 m x 5 m to about 8 m x 15 m. Pinkish feldspar (that is, potassium feldspar) is the dominant mineral in the granite gneiss and the pegmatite. This implies that its weathered product will be rich in clay. The rock types found here are believed to be part of older granite suite and are mostly exposed along the river channels where they appear in most cases weathered. Based on the relative grain size, the major rock types are (i) porphyritic coarse-grained granite, and (ii) medium to fine-grained granite. The former are mostly flat-lying with sizes ranging from few metres to about thirty metres. They are believed to continuously underlay the region that is covered by the thick overburden and are found outcropping along the river channels. Owing to biological weathering, the outcrops are broken into boulders. The latter are also flat-lying along the river channels and relatively high rising elongated outcrops on the surface, and unlike the pophyritic granite they are less weathered. The rocks are found in east-west (E-W) treading veins and joints which are sometimes filled by aplitic or quartz; this is in contrast to the porphyritic granite that are found in the north-south (N-S) trending quarts and aplitic veins ranging in length from 2 m to about 15 m. The medium to fine-grained granitic rocks are broken up into boulders in some places and they show the effect of weathering in the form of colour change and loose rock fragments (Adesoye, 1986).

A brief note on the hydrogeologic history of the area of study is referenced in the report that the aquifer system in the local Basement Complex of which this area is a tranche

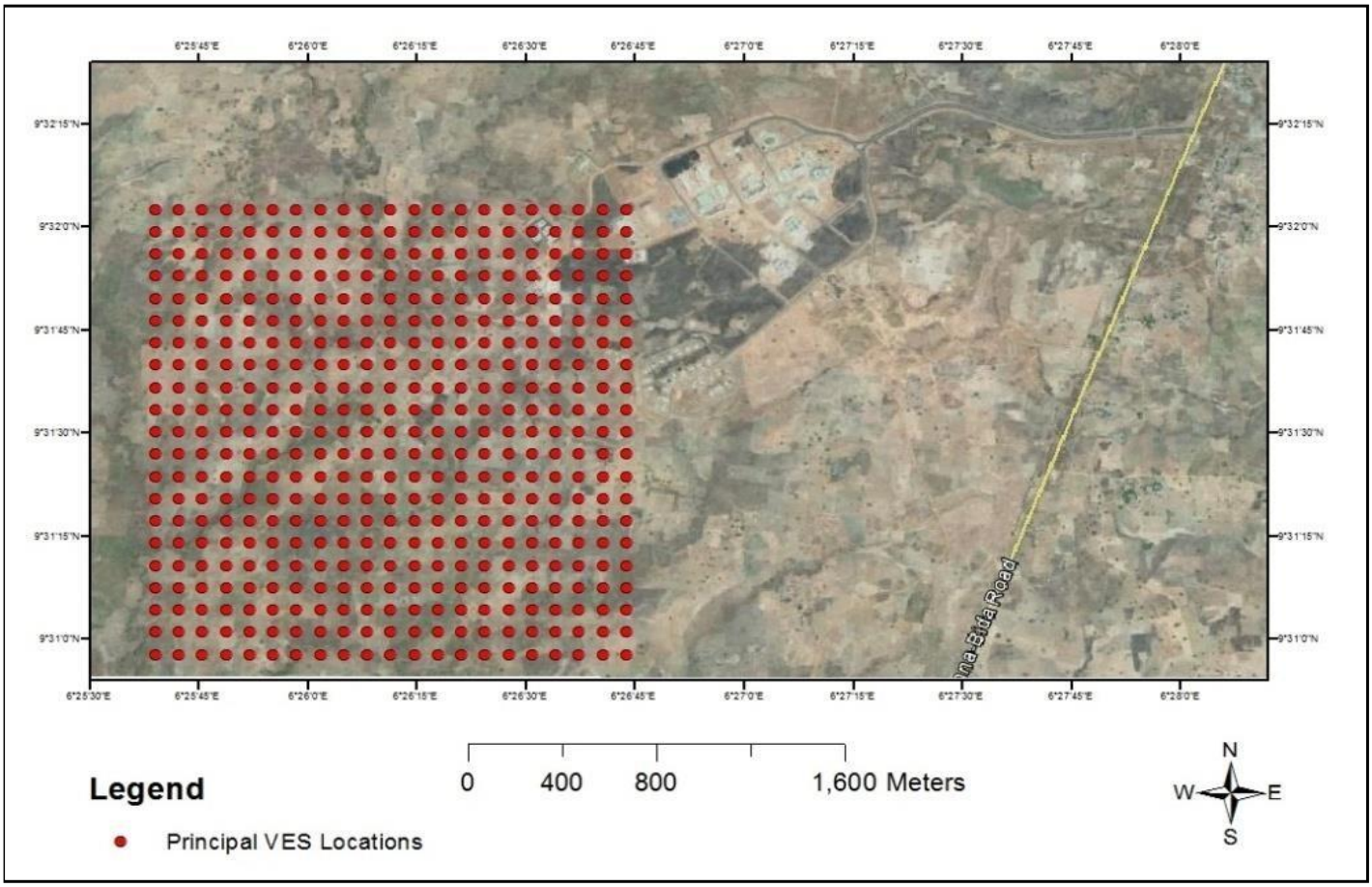

Figure 1. Grid of the 4 km^2 tranche at 100 m station-spacing (The tadpole-shaped feature is Phase I, the present developed portion of the GKC, seen to the northeast; the Minna-Bida Road is seen as the linear slope to the far east of the grid).

consists of weathered and fractured basement rocks (Salako and Udensi, 2005; Udensi et al., 2006). Further, where the fractured zones are saturated, relatively high yield of groundwater can be sustained from boreholes penetrating such a sequence. Furthermore, Salako and Udensi (2005) pointed out that a minimum overburden thickness of 15 m over the weathered and fractured basement would suffice to form an aquifer. However, there is an informal and unstated rule concerning the local Basement Complex area that where schist outcrops occur (and they are very few and far between at the area of study), fracturing of the underlying bedrock is a distinct possibility. Actually, Jonah and Adebayo (2019) concerned themselves with correlating these presently much-weathered schist bodies with the predominantly-identified aquifer prospects at the area of study along the diagonals of the fault-trace of fracture signatures (Figure 16).

The 4 km^2 dual VES-IP survey

The corpus of data-field for the 4 km^2 dual VES-IP survey was collected for a field layout of the Schlumberger array at 100 m station-spacing and 100 m profile-spacing over a three-year period. The survey trend was an east-west (or transverse traverse, TT) sense for individual stations. Principal profile lines are in the north-south direction (or longitudinal traverse, LT) with the first profile line being the westernmost line of longitude: numerical station-designation is from west to east; the profile “lines” in Figure 2 are the linear alignment of the red dots at 100 m spacing. Actual cross-profile progressive increment proceeded from south to north, thus the first assigned station of survey based on this format is the most extreme southwestern point in the 2 km by 2 km grid appropriately called P1-1; that is, Station 1 of Profile 1. Station 2 of Profile 1 (P1-2) is exactly 100 m to the north of Station 1; Station 3 of Profile 1 (P1-3) is exactly 100 m to the north of Station 2 and exactly 200 m north of Station 1, and so on. P2-1 means Station 1 of Profile 2; this is exactly 100 m to the east of P1-1; P3-1 is exactly 100 m to the east of P2-1 and exactly 200 m to the east of P1-1. At each station of survey, cables were appropriately laid out in conformance with the Schlumberger array and the survey crew proceeded to take 21 sequences of tandem VES and IP measurements. Depending on the numbers of field hands and the

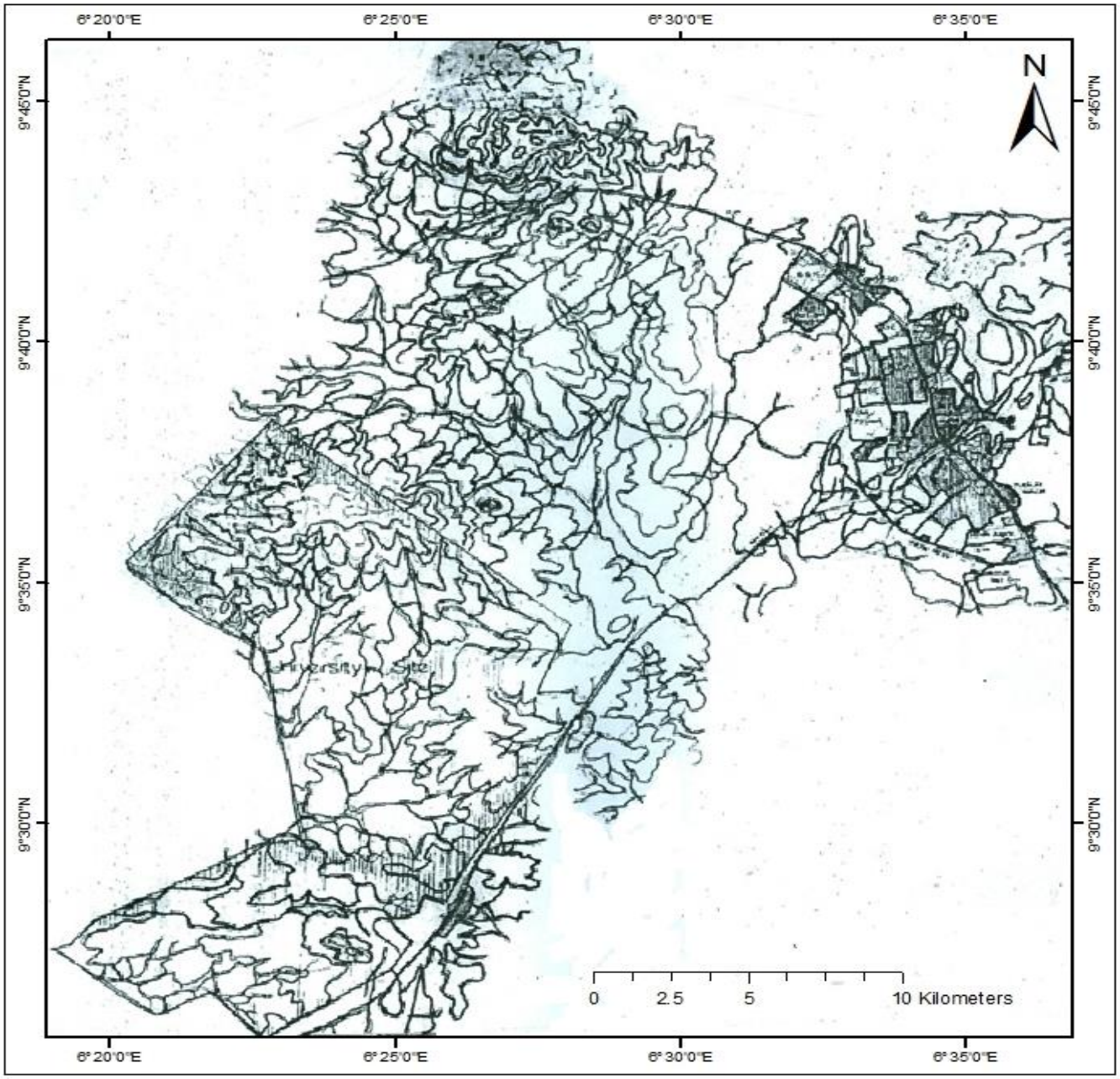

Figure 2. The Gidan Kwano Campus lies southwest of Minna.

condition of the bush paths through which cables will be laid (when the rains come, thick undergrowths and water-logged terrains make it very difficult to lay cables), it is observed that an interval of two and a half hours is expended between commencing measurements at adjacent survey points along an east-west traverse. Not all the 441 principal survey stations for the 4 km^2 areal extent were occupied during the course of survey because of barriers encountered at coincident points of surveys; the barriers are those due to wet-stream, outcrop, thicket, built-up area, instrumental error, and raw sewage. The schedule of Figure 2 has been colour-coded to indicate the stations that were occupied for data collection during the course of this survey, see Figure 3.

Data-field of the dual VES-IP survey

Of the 441 (21 x 21) total VES and IP stations-in-tandem for the 2 km x 2 km grid at 100 m station-spacing, only a total of *circa* 309 points were occupied owing to constraints of raw sewage pollution and built-up land areas encountered during the course of the survey. The 21 sequences of measurements for a station, for the VES

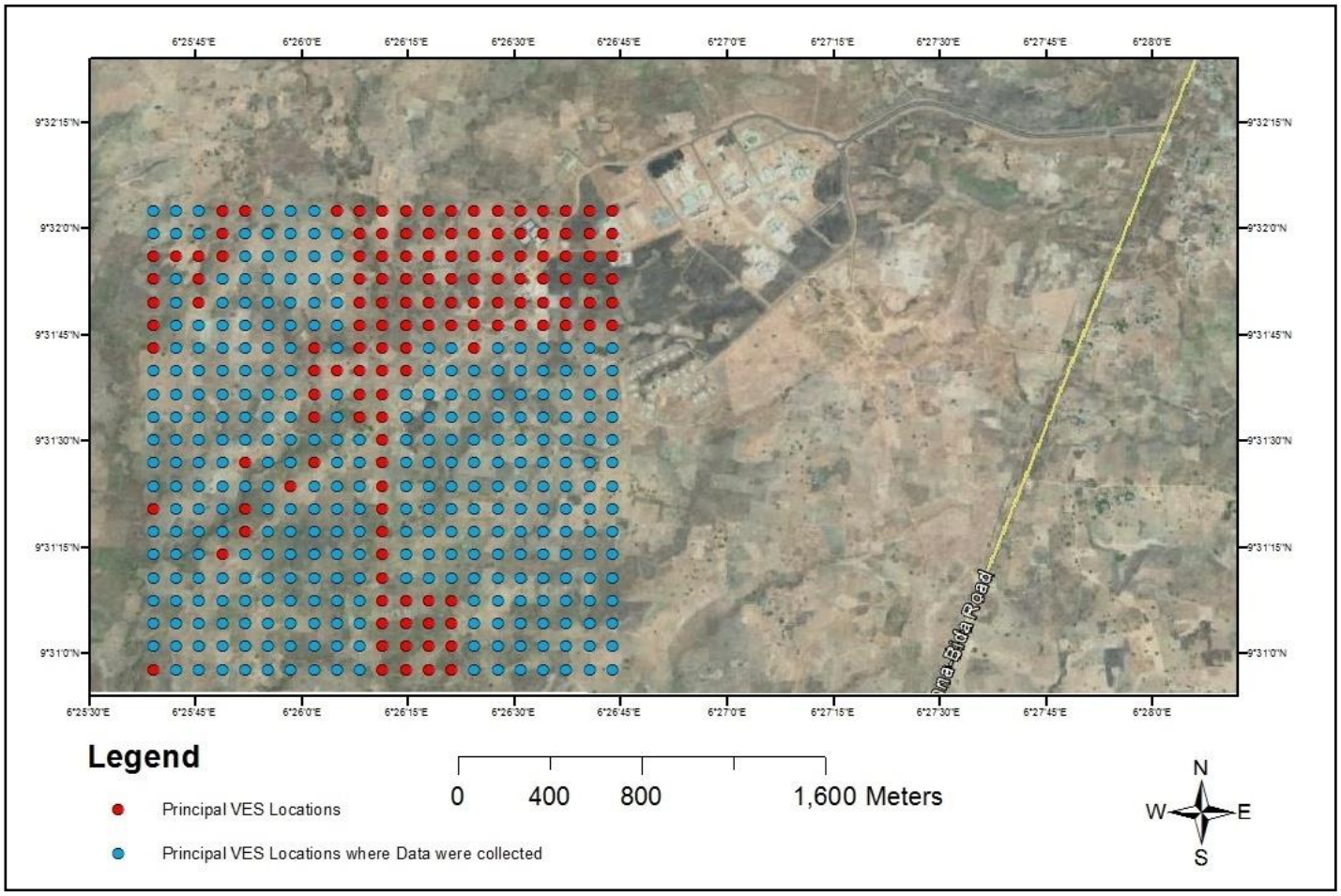

Figure 3. Locations of the principal stations of the 4 km^2 tranche colour-coded for locations where data was collected.

phase and for the IP phase, were tabulated in a purpose-specific format for each station. The table header provided information on the type of survey, the mode of survey, the configuration array, the location of survey, weather, equipment type, plus the transverse traverse station designation. The columns of the body-of-table contain information about sequential half current-electrode and half potential-electrode spacing, geometric factor, measured resistance values, and the computed resistivity values.

Data processing

The field resistivity values were initially subjected to the log-log plot routine of the Windows-compatible WinResist® software whence corresponding field curves for all the stations occupied were produced. Each of the WinResist® log-log plot provides information on the numbers of layers, the average resistivity values of these layers, and their approximate thicknesses. Also, in order to show variation of resistivity on a constant plane across the 4 km^2 area of study for the VES survey, resistivity maps at constant depths (that is, iso-resistivity maps) were generated at the 1, 10, 20, 30, 40, 50, 60, 70, 80, 90, and 100 m depth points. Now, in order to show variation of overburden thickness (that is, depth-to-basement) on a constant plane across the 4 km^2 area of study for the VES survey, an isopach map with its equivalent DEM map were produced for the 4 km^2 area of study under consideration.

RESULTS

Production of the log-log plots: The WinResist® log-log plots and corresponding data-field for P1-6, P2-1, and P3-9 have been reproduced herein out of a total of *circa* 309 plots and these are shown as Figures 4 to 6.

Production of the geoelectric cross-sections: In order to show the profile of the variation of resistivity with its associated actual number of layers at each VES survey station along the perpendicular north-south traverses, geoelectric cross-sections derivable from analyses of the

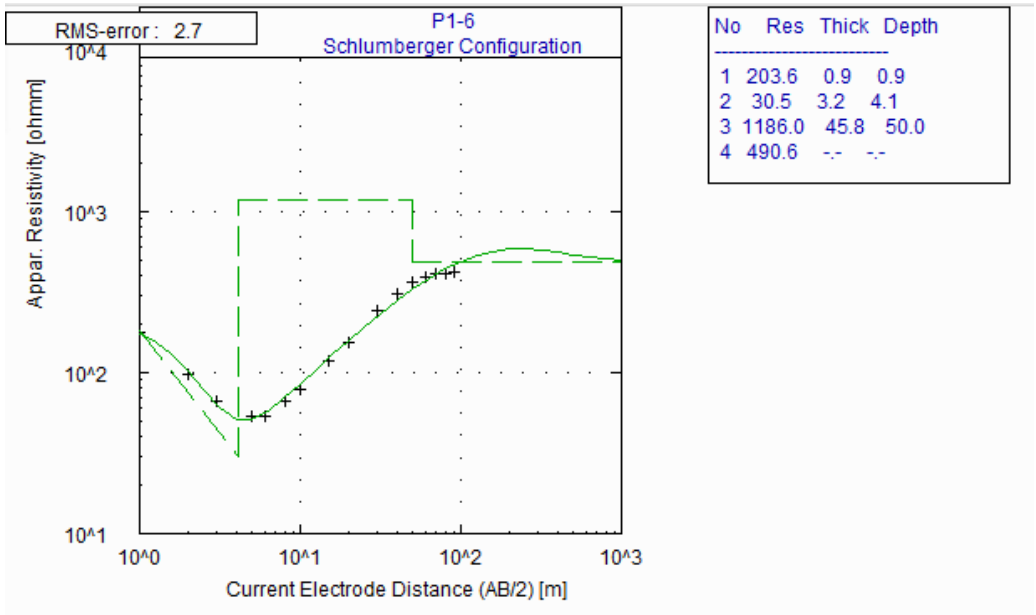

Distance	Resistivity	No	Var
1.00	179.0000	1	-----
2.00	97.0000	2	-----
3.00	67.0000	3	-----
5.00	53.0000	4	-----
6.00	53.0000	5	-----
8.00	66.0000	6	-----
10.00	79.0000	7	-----
15.00	119.0000	8	-----
20.00	154.0000	9	-----
30.00	243.0000	10	-----
40.00	309.0000	11	-----
50.00	362.0000	12	-----
60.00	396.0000	13	-----
70.00	408.0000	14	-----
80.00	414.0000	15	-----
90.00	425.0000	16	-----

Figure 4. WinResist® plot and corresponding data-field for P1-6.

WinResist® log-log plots were generated for 20 profiles; the geoelectric cross-sections of only P1, P2, and P3 are shown as Figures 7 to 9.

Production of the pseudosection plots: In order to show the resistivity cross-section along a perpendicular north-south traverse, the Surfer-11® application was used to produce the equivalent pseudosections and these were generated for 20 profiles. The pseudosection plots of only P1, P2, and P3 are shown as Figures 10 to 12.

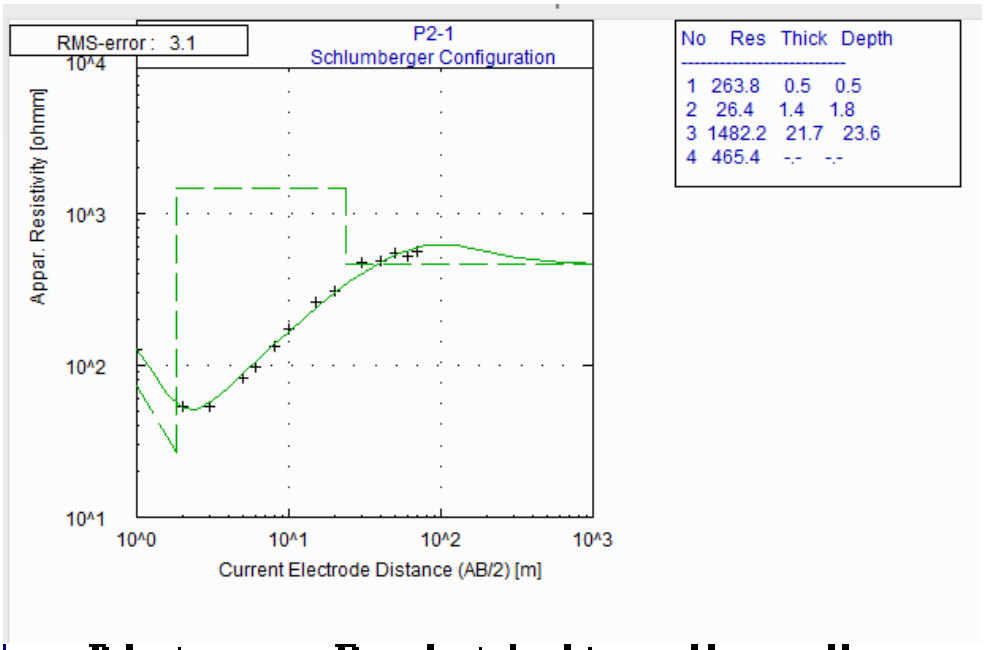

Distance	Resistivity	No	Var
1.00	126.0000	1	------
2.00	53.0000	2	------
3.00	53.0000	3	------
5.00	82.0000	4	------
6.00	98.0000	5	------
8.00	134.0000	6	------
10.00	174.0000	7	------
15.00	258.0000	8	------
20.00	307.0000	9	------
30.00	481.0000	10	------
40.00	487.0000	11	------
50.00	547.0000	12	------
60.00	520.0000	13	------
70.00	564.0000	14	------

Press Space Bar

Figure 5. WinResist® plot and Corresponding Data-field for P2-1.

Production of Iso-resistivity maps at depths: In order to show the variation of resistivity on a constant plane across the 4 km^2 area of study for the VES survey, it is necessary to produce resistivity maps at constant depths (that is, the iso-resistivity maps). For this study, the Surfer®11 software was used to generate iso-resistivity maps at 1, 10, 20m, 30, 40, 50, 60, 70, 80, 90, and 100 m; only the maps for the 80, 90, and 100 m depth points are

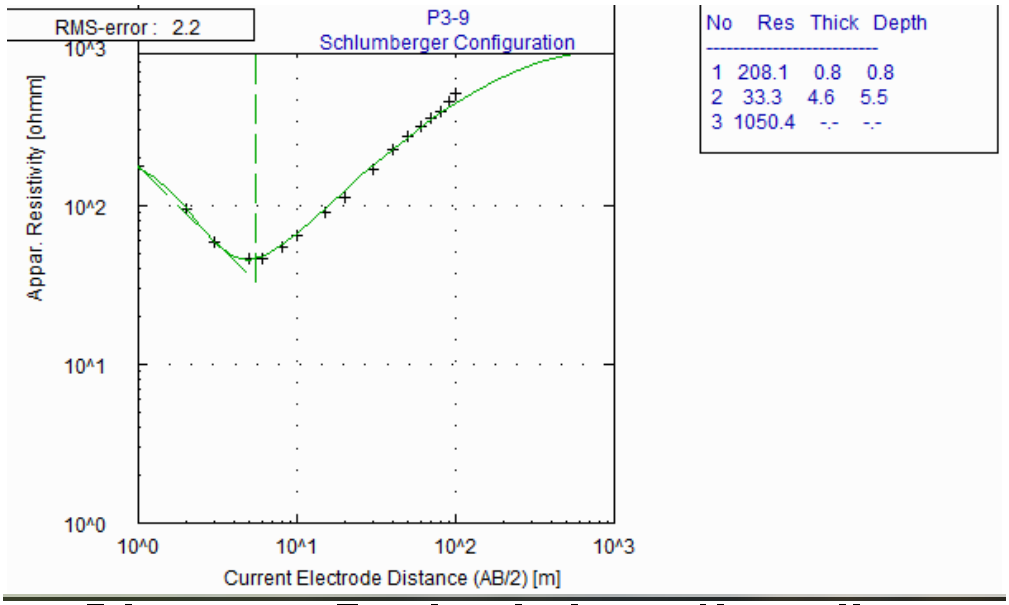

Distance	Resistivity	No	Var
1.00	178.0200	1	------
2.00	95.0930	2	------
3.00	59.0050	3	------
5.00	46.4610	4	------
6.00	46.9580	5	------
8.00	55.4360	6	------
10.00	64.9070	7	------
15.00	90.8760	8	------
20.00	113.6800	9	------
30.00	170.5800	10	------
40.00	228.1750	11	------
50.00	270.7600	12	------
60.00	314.7100	13	------
70.00	353.4100	14	------
80.00	396.9250	15	------
90.00	450.0000	16	------
100.00	508.0600	17	------

Figure 6. WinResist® plot and Corresponding Data-field for P3-9.

presented herein as Figures 13 to 15.

Induced polarization (IP) validation of fracture signatures inferred from the geoelectric cross-sections of some sample locations: The concurrently-acquired IP tables for P3-1 and P3-3 are presented (out of a total of *circa* 309 tables) as Tables 1 and 2.

DISCUSSION

The geoelectric cross-section of P1: A three-layer geological sequence is defined for P1, characteristic of the geology of the area of study and its wider environs; these three layers are the topsoil, the weathered zone, and the fresh basement. These three layers are the predominant

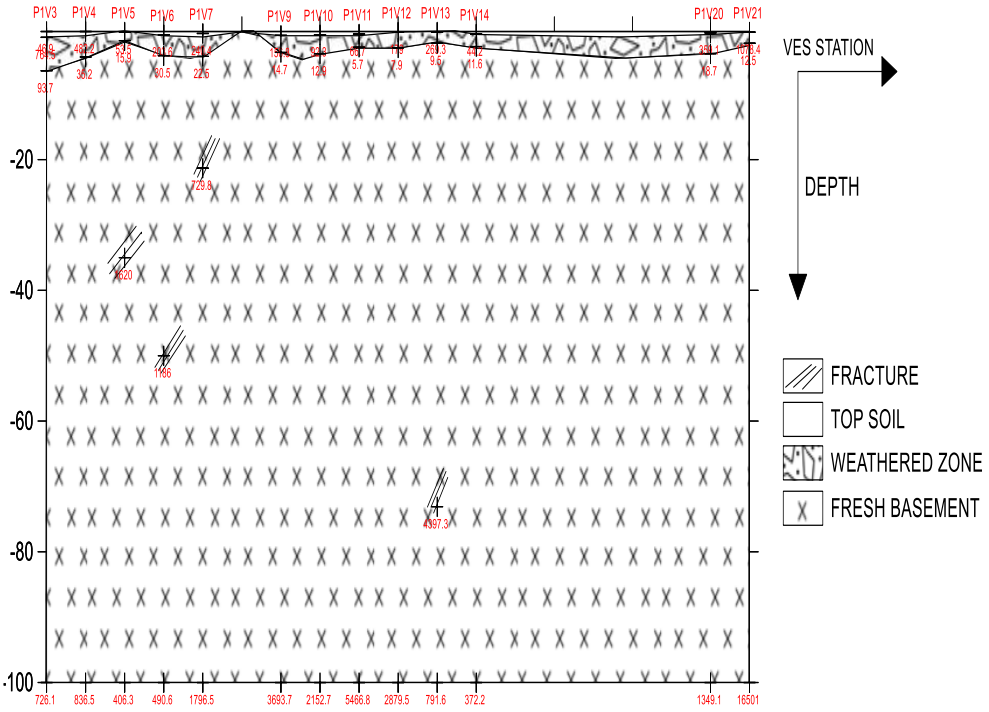

Figure 7. Geoelectric cross-section of P1.

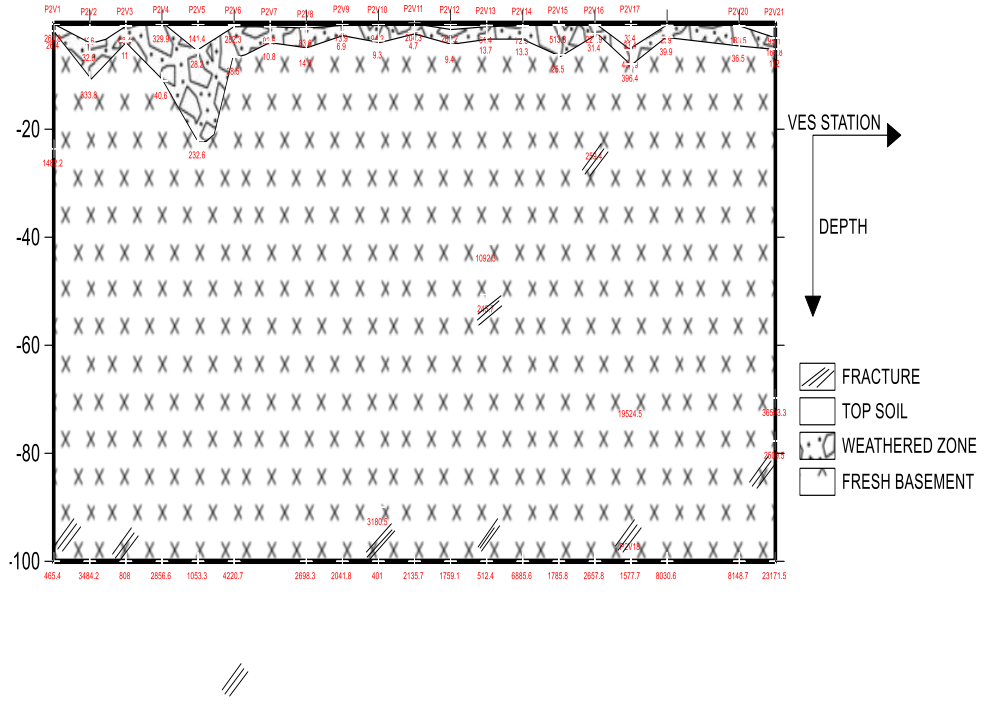

Figure 8. Geoelectric cross-section of P2.

ones even though the WinResist® log-log plots for the different survey stations of P1 may indicate more than three layers for each point. Subsurface fractures occur beneath P1-5 at the 35 m depth-mark, P1-6 at the 50 m depth-mark, P1-7 at the 4 m depth-mark down to the 21 m depth-mark, and P1-13 at the 73 m depth-mark.

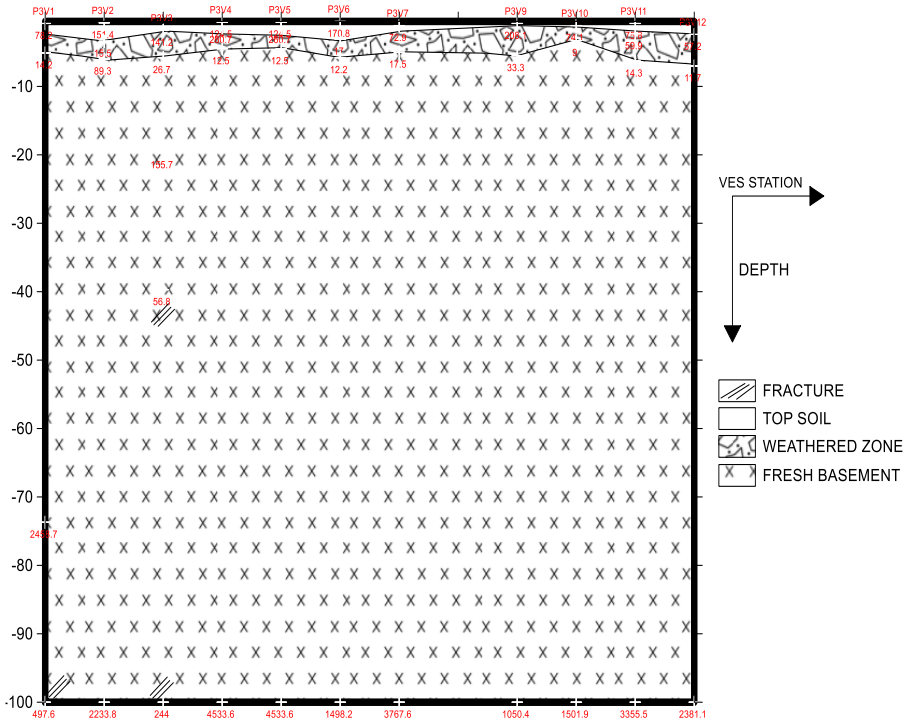

Figure 9. Geoelectric cross-section of P3.

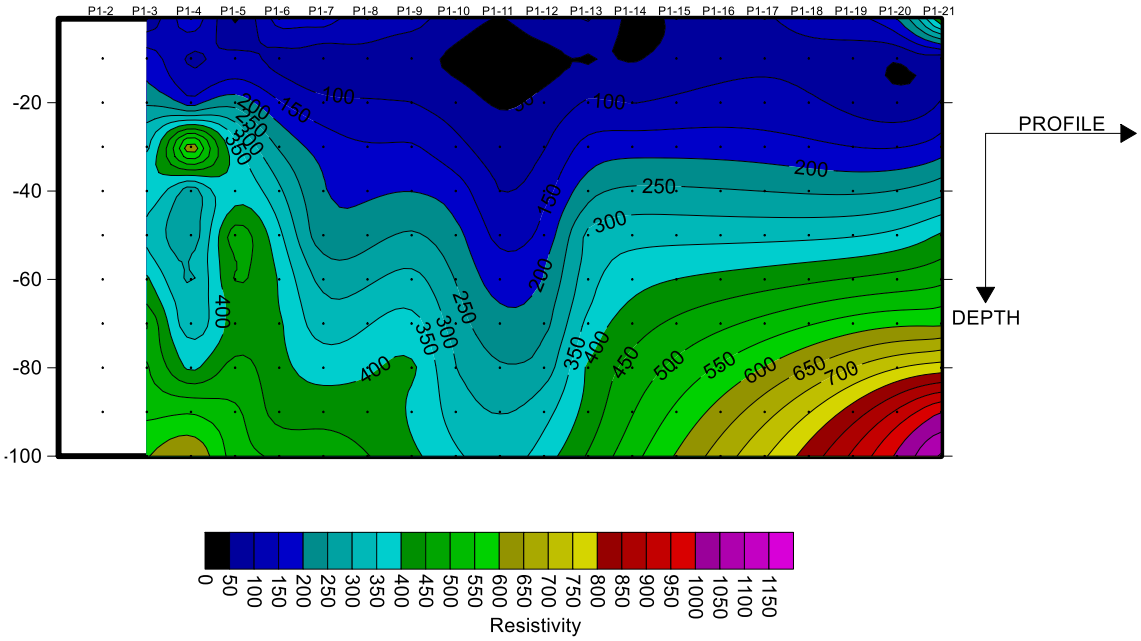

Figure 10. Pseudosection plot for P1.

The geoelectric cross-section of P2: A three-layer geological sequence is also defined for P2; these three layers are the topsoil, the weathered zone, and the fresh basement. Subsurface fractures occur beneath P2-1 at the 24 m depth-mark, P2-10 at the 100 m depth-mark, P2-13 at the 41 m depth-and 51 m depth-marks, and P2-16 at the 2 m depth-mark (of 20 m thickness).

The geoelectric cross-section of P3: The three-layer sequence of topsoil, the weathered zone, and fresh

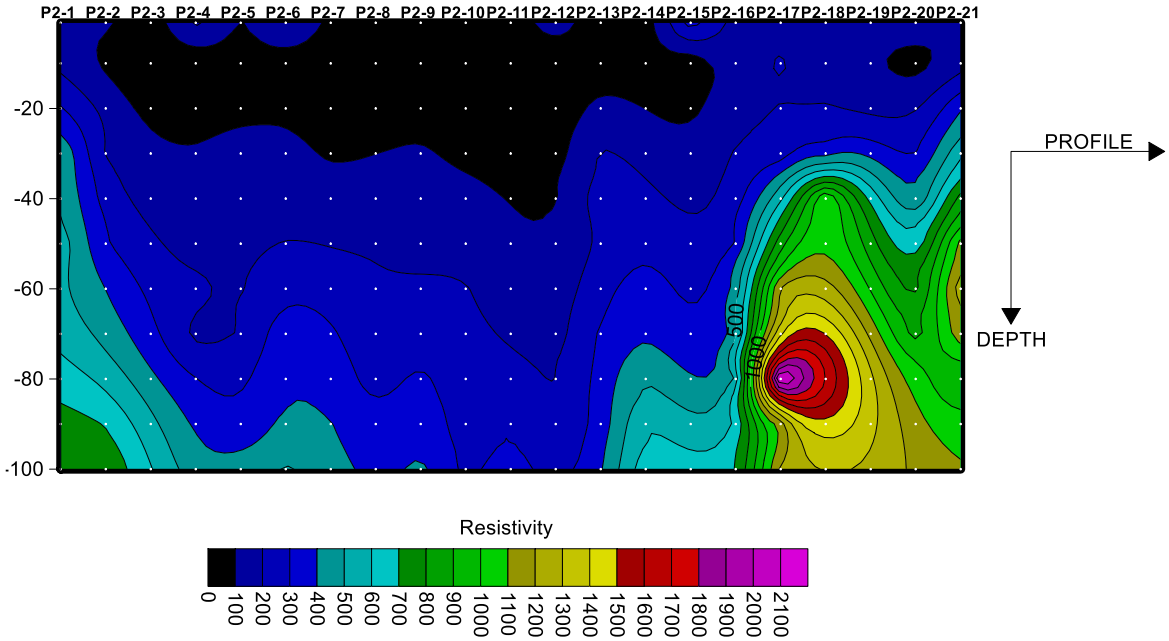

Figure 11. Pseudosection plot for P2.

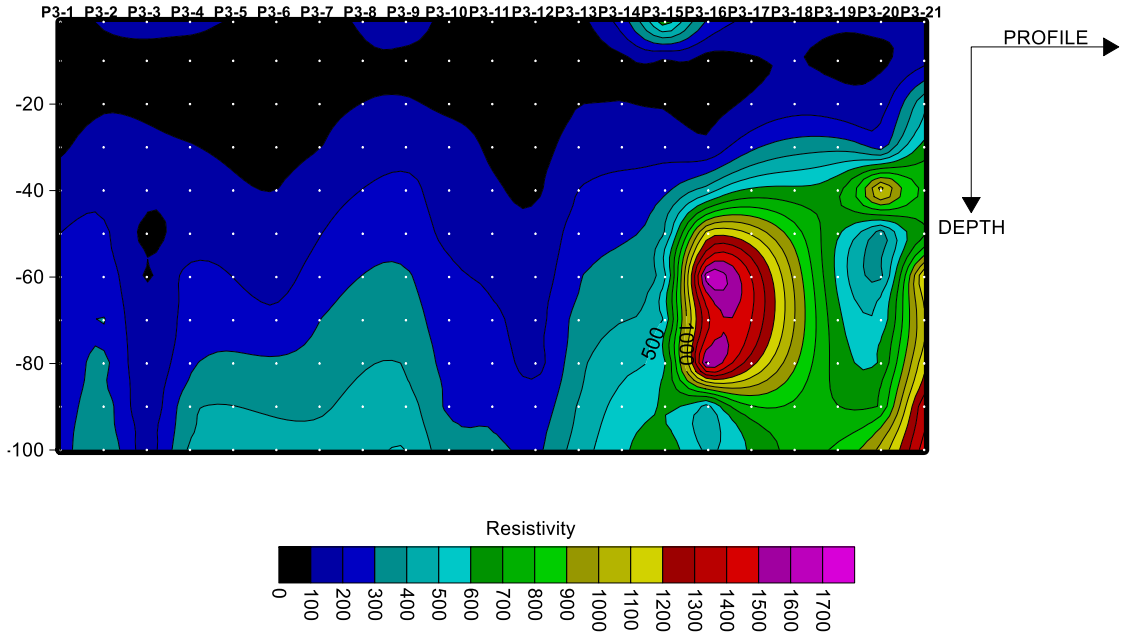

Figure 12. Pseudosection plot for P3.

basement is also defined for P3. Subsurface fractures occur beneath P3-1 at the 74 m depth-mark and P3-3 at the 20 m depth- and 40 m depth-marks.

The geoelectric cross-section of P4: The three-layer sequence of topsoil, the weathered zone, and fresh basement is also defined for P4. Subsurface fractures occur beneath P4-1 at the 10 m depth-mark, P4-5 at the 44 m depth-mark, and the P4-9 at the 29 m depth- and 48 m depth-marks.

The geoelectric cross-section of P5: The three-layer sequence of topsoil, the weathered zone, and fresh basement is also defined for P5. Subsurface fractures occur beneath P5-2 at the 3 m depth-mark (down to the 21 m depth-mark) and P5-12 at the 100 m depth-mark.

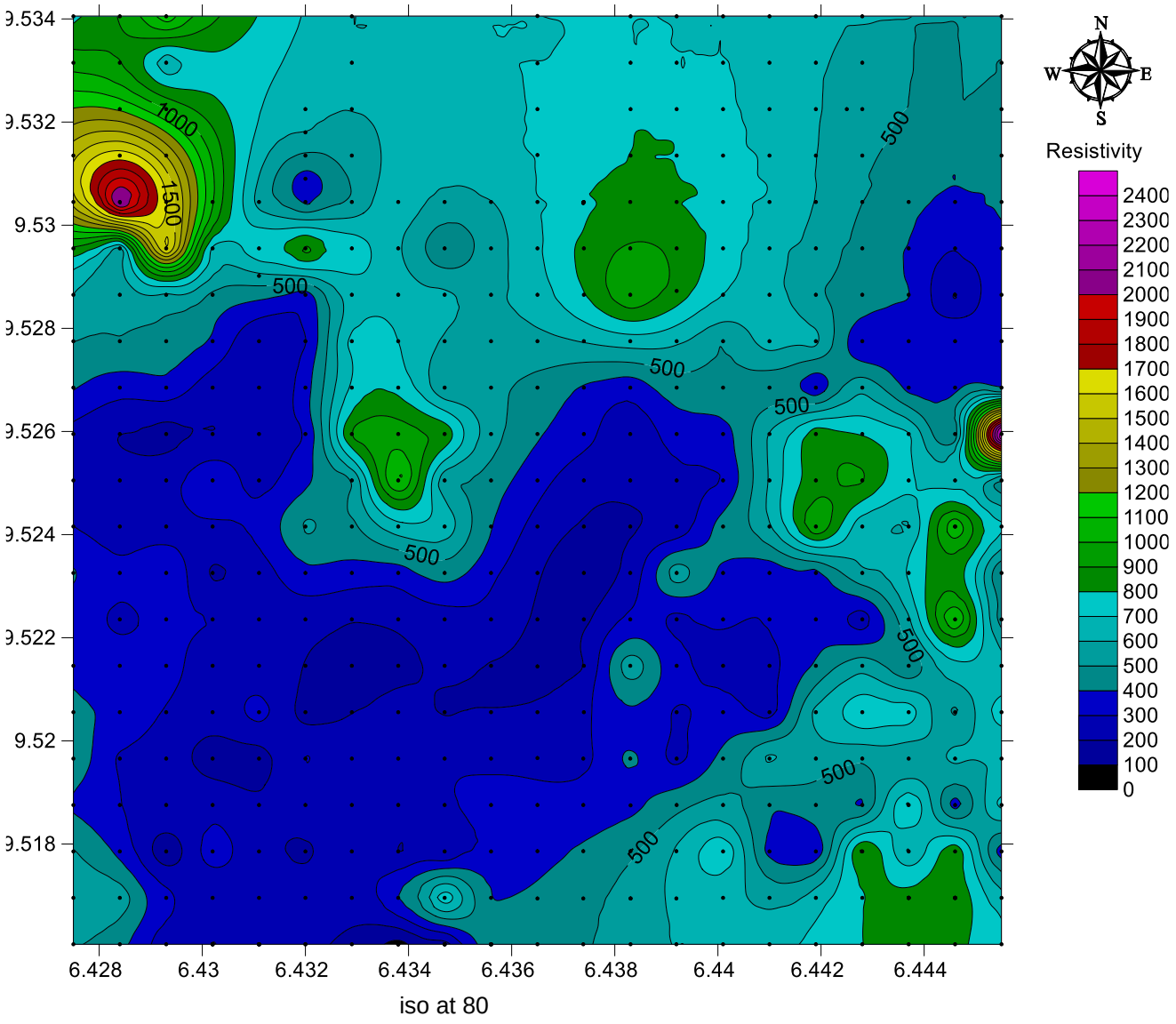

Figure 13. Iso-resistivity map at 80 m.

The geoelectric cross-section of P6: The three-layer sequence of topsoil, the weathered zone, and fresh basement is also defined for P6. Subsurface fractures occur beneath P6-2 at the 73 m depth-mark, P6-3 at the 26 m depth-mark, P6-11 at the 37 m depth-mark, P6-13 at the 6 m depth-mark, P6-16 at the 84 m depth-mark, P6-19 at the 100 m depth-mark, and P6-20 at the 100 m depth-mark.

The geoelectric cross-section of P7: The three-layer sequence of topsoil, the weathered zone, and fresh basement is also defined for P7. Subsurface fractures occur beneath P7-16 at the 40 m depth-mark.

The geoelectric cross-section of P8: The three-layer sequence of topsoil, the weathered zone, and fresh basement is also defined for P8. Subsurface fractures occur beneath P8-1 at the 40 m depth-mark, P8-18 at the 68 m depth- and 78 m depth-marks, and P8-21 at the 28 m depth-mark.

The geoelectric cross-section of P9: The three-layer sequence of topsoil, the weathered zone, and fresh basement is also defined for P9. Subsurface fractures occur beneath P9-1 at the 5 m depth-mark, P9-3 at the 39 m depth-mark, and P9-8 at the 80 m depth-mark.

The geoelectric cross-section of P10: The three-layer sequence of topsoil, the weathered zone, and fresh basement is also defined for P10. Subsurface fractures occur beneath P10-1 at the *circa* 100 m depth-mark and P10-7 at the 28 m depth-mark.

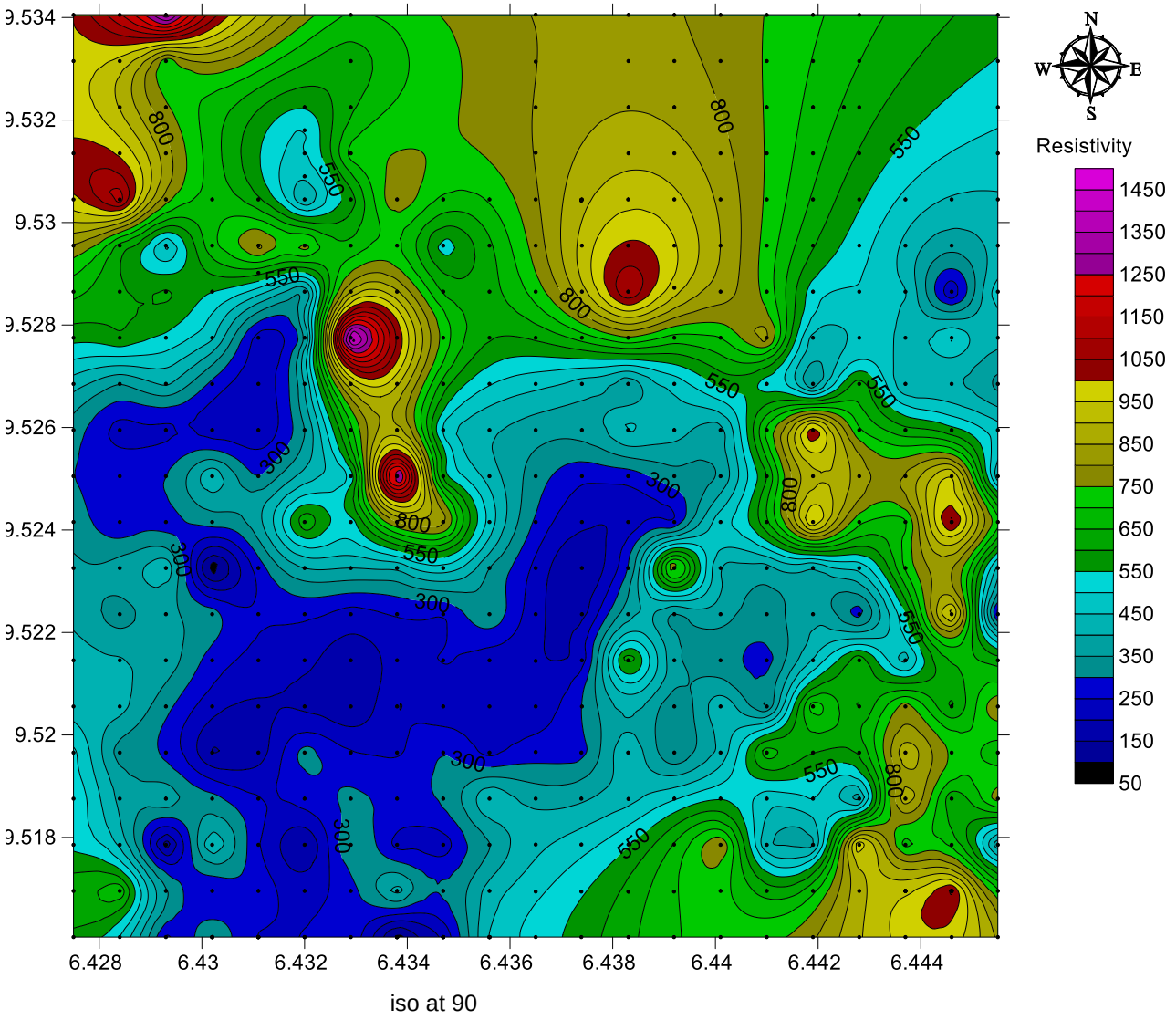

Figure 14. Iso-resistivity map at 90 m.

The geoelectric cross-section of P12: The three-layer sequence of topsoil, the weathered zone, and fresh basement is also defined for P12. Subsurface fractures occur beneath P12-8 at the 92 m depth-mark and P12-11 at the 95 m depth-mark.

The geoelectric cross-section of P13: The three-layer sequence of topsoil, the weathered zone, and fresh basement is also defined for P13. Subsurface fractures occur beneath P13-8 at the 6 m depth-mark and P13-10 at the 19 m depth-mark.

The geoelectric cross-section of P14: The three-layer sequence of topsoil, the weathered zone, and fresh basement is also defined for P14. Subsurface fractures occur beneath P14-8 at the 17 m depth-mark and P14-9 at the 5 m depth-mark (down to the 18 m depth-mark).

The geoelectric cross-section of P15: The three-layer sequence of topsoil, the weathered zone, and fresh basement is also defined for P15. Subsurface fractures occur beneath P15-3 at the 79 m depth-mark (down to the 99 m depth-mark) and P15-4 at the 15 m depth-mark.

The geoelectric cross-section of P16: The three-layer sequence of topsoil, the weathered zone, and fresh basement is also defined for P16. Subsurface fractures occur beneath P16-12 at the 4 m and 18 m depth-marks (down to the 30 m depth-mark).

The geoelectric cross-section of P17: The three-layer sequence of topsoil, the weathered zone, and fresh basement is also defined for P17. Subsurface fractures occur beneath P17-6 at the 11 m depth-mark (down to the 29 m depth-mark), P17-8 at the 6 m depth-mark (down to

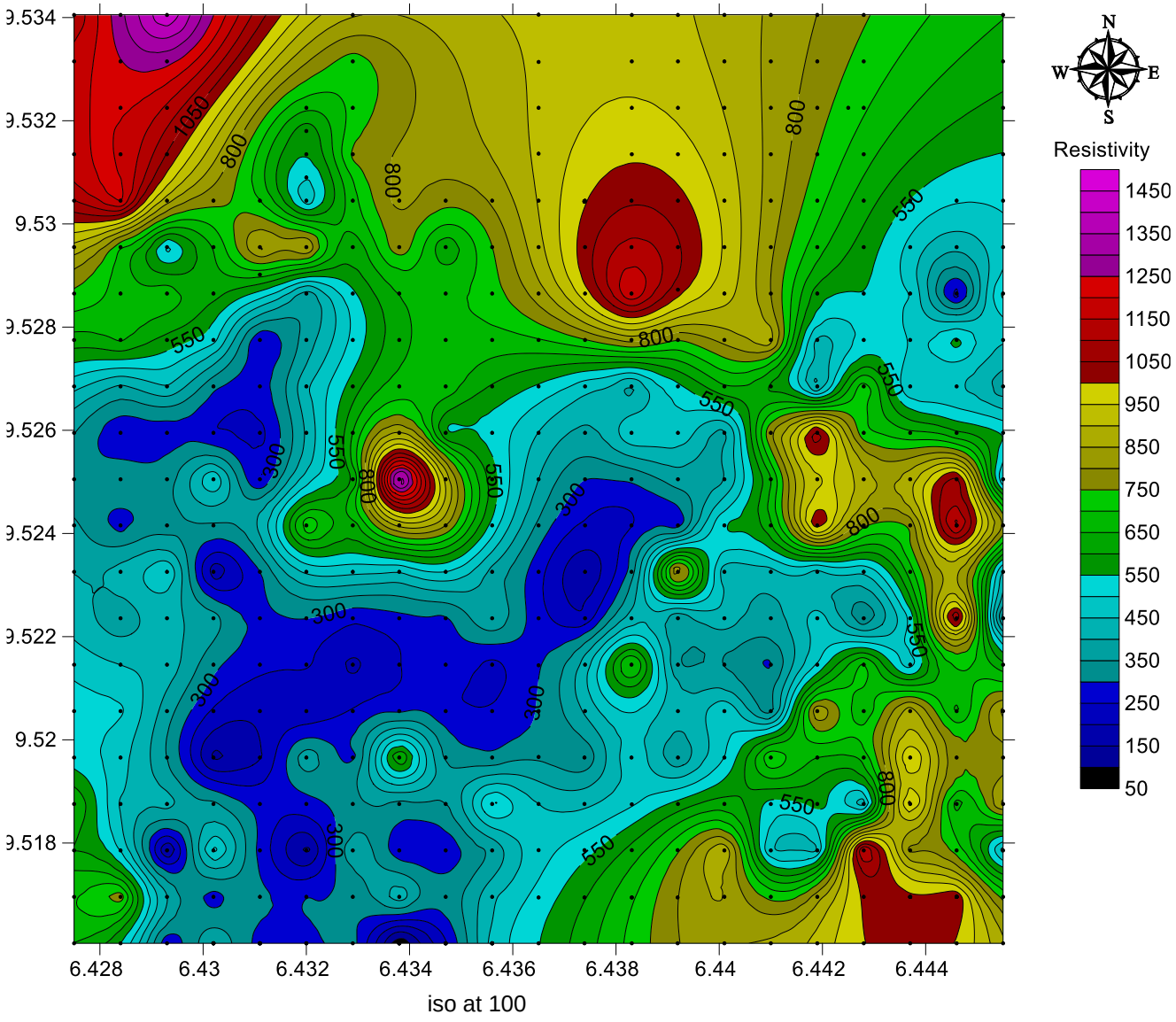

Figure 15. Iso-resistivity map at 100 m.

the 31 m depth-mark), P17-11 at the 8 m depth-mark (down to the 36 m depth-mark), P17-12 at the 6 m depth-mark (down to the 19 m depth-mark), P17-13 at the 84 m depth-mark, P17-14 at the 89 m depth-mark, and P17-15 at the comparative shallow depth of 6 m.

The geoelectric cross-section of P18: The three-layer sequence of topsoil, the weathered zone, and fresh basement is also defined for P18. Subsurface fractures occur beneath P18-7 at the 10 m depth-mark (down to the 22 m depth-mark), P18-8 at the 12 m depth-mark, P18-9 at the 24 m depth-mark, and P18-12 at the 15 m depth-mark (down to the 42 m depth-mark).

The geoelectric cross-section of P19: The three-layer sequence of topsoil, the weathered zone, and fresh basement is also defined for P19. Subsurface fractures occur beneath P19-7 at the 64 m depth-mark, P19-8 at the 81 m depth-mark, P19-12 at the 53 and 73 m depth-marks, and P19-15 at the 27 m depth-mark.

The geoelectric cross-section of P20: The three-layer sequence of topsoil, the weathered zone, and fresh basement is also defined for P20. Subsurface fractures occur beneath P20-4 at the 7 m and 15 m (down to the 22 m) depth-marks, P20-12 at the 2 m and 28 m (down to the 46 m) depth-marks, and P20-15 at the 7 m depth-mark.

The geoelectric cross-section of P21: The three-layer sequence of topsoil, the weathered zone, and fresh basement is also defined for P21. Subsurface fractures occur beneath P21-4 at 1 m (down to the 23 m depth-

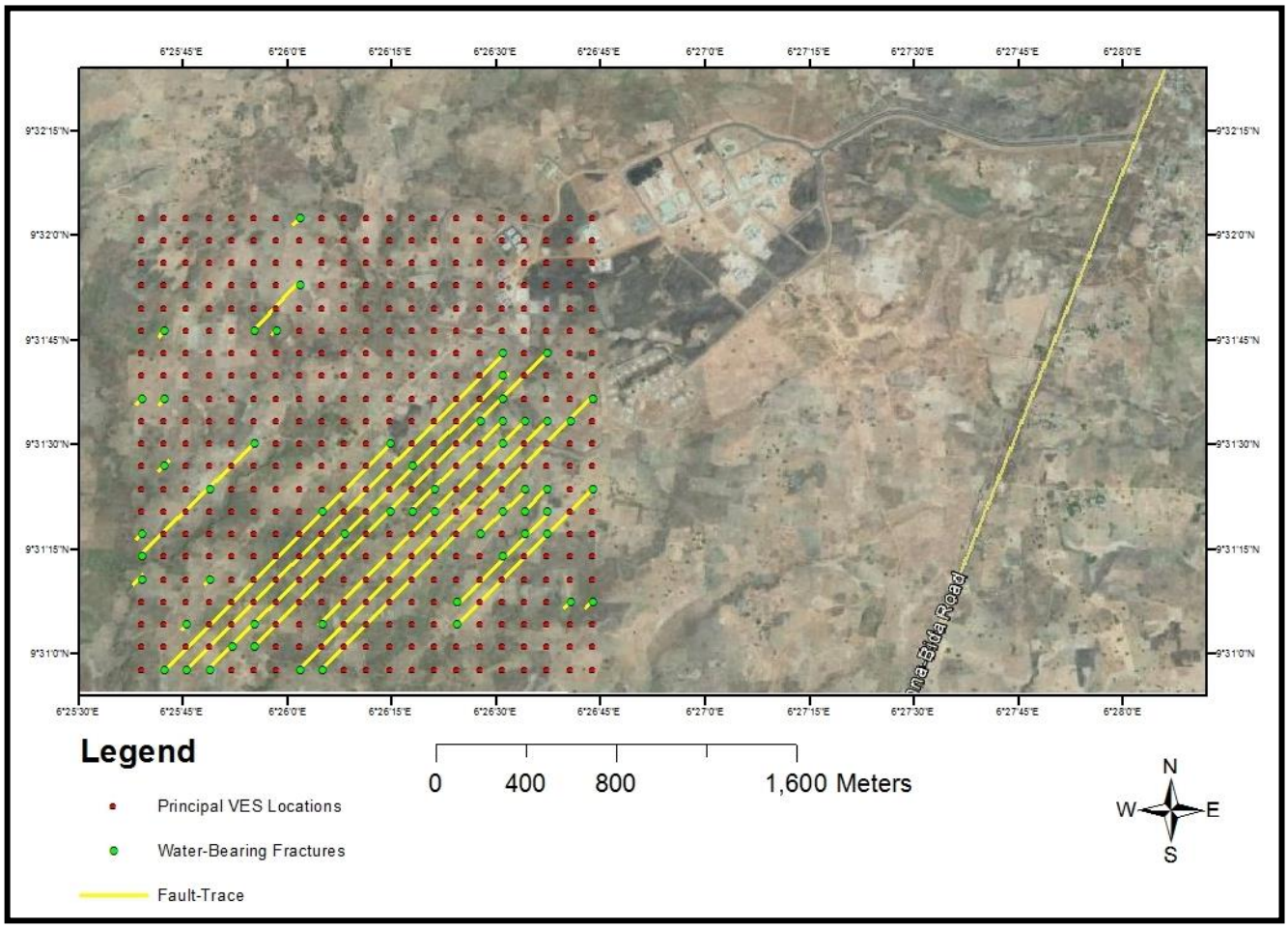

Figure 16. Fault-trace of fracture signatures inferred from a combination of the geoelectric cross-sections and the induced polarisation tables on the satellite imagery map of the area of study with the developed Phase I in the background.

mark), P21-8 at the 2 m depth-mark, P21-9 at the 60 m depth-mark, P21-11 at the 4 m depth-mark, P21-12 at the 29 m depth-mark, and P21-13 at the 25 m depth-mark.

Observation arising from IP validation of P3

On P3-1 at the 74 m depth-mark (Table 1): The chargeability of -9.19 msat 80 m (>74 m) confirms the information gleaned from the log-log plot about the existence of a low-resistivity zone at this depth. The absolute value of the chargeability of -9.19ms at the 80 m (>74 m) depth (that is, 9.19) is “significant” with respect to the other absolute values of chargeability observed at P3-1. Thus, P3-1 is considered a water-bearing fracture.

On P3-3 at the 20m depth-and40m depth-marks (Table 2): The chargeability values of -1.23ms at 20 m and -5.73 at 40 m confirm the information gleaned from the log-log plot about the existence of low-resistivity zones at these depths. Thus, P3-3 is considered a water-bearing fracture.

Water-bearing fracture signatures inferred from a combination of the geoelectric cross-sections and the induced polarisation Tables

Along the First North-South Profile (P1):
P1-5 ($09^0 31' 10.76''$; $006^0 25' 39.00''$)
P1-6 ($09^0 31' 14.00''$; $006^0 25' 39.00''$)
P1-7 ($09^0 31' 17.24''$; $006^0 25' 39.00''$)
P1-13 ($09^0 31' 36.66''$; $006^0 25' 39.00''$)

Along the Second North-South Profile (P2):
P2-1 ($09^0 30' 57.80''$;$006^0 25' 42.24''$)
P2-10 ($09^0 31' 26.96''$; $006^0 25' 42.24''$)
P2-13 ($09^0 31' 36.66''$; $006^0 25' 42.24''$)
P2-16 ($09^0 31' 46.38''$; $006^0 25' 42.24''$)

Along the Third North-South Profile (P3):
P3-1 ($09^0 30' 57.80''$; $006^0 25' 45.48''$)
P3-3 ($09^0 31' 04.28''$; $006^0 25' 45.48''$)

Along the Fourth North-South Profile (P4):

Table 1. Tandem IP table for VES P3-1.

AB/2 (Current)	MN/2 (Potential)	Geom. factor, K	Chargeability	Standard Deviation	Current (I)	Stacks
1	.50	2.36	0.40	0.04	100mA	4
2	.50	11.8	0.39	0.09	100mA	4
3	.50	27.8	0.61	0.21	50mA	4
5	.50	77.8	1.33	3.80	50mA	4
6	.50	112	2.47	0.13	50mA	4
6	1.00	55	6.37	6.10	50mA	4
8	1.00	99	2.90	0.19	50mA	4
10	1.00	156	-18.9	6.00	50mA	4
10	2.50	58.9	4.01	1.40	50mA	4
15	2.50	137	0.56	29.0	50mA	4
20	2.50	245	3.07	0.63	50mA	4
30	2.50	562	8.73	4.80	50mA	4
40	2.50	1001	1.50	2.10	50mA	4
40	7.50	323	-0.90	0.62	50mA	4
50	7.50	512	-0.34	3.60	50mA	4
60	7.50	742	3.14	4.50	100mA	4
70	7.50	1014	1.24	6.90	100mA	4
80	7.50	1329	**-9.19**	0.71	50mA	4
80	15.00	647	11.9	2.20	50mA	4
90	15.00	825	1.13	0.32	100mA	4
100	15.00	1024	0.80	0.30	100mA	4

Table 2. Tandem IP table for VES P3-3.

AB/2 (m) (Current)	MN/2 (m) (Potential)	Geom. factor, K	Chargeability	Standard Deviation	Current (I)	Stacks
1	.50	2.36	1.19	0.07	100mA	4
2	.50	11.8	0.63	0.01	50mA	4
3	.50	27.8	0.64	0.03	50mA	4
5	.50	77.8	0.70	0.07	100ma	4
6	.50	112	-0.30	0.92	20mA	4
6	1.00	55	3.81	29.0	20mA	4
8	1.00	99	3.98	1.60	20mA	4
10	1.00	156	0.40	1.30	100mA	4
10	2.50	58.9	1.63	0.52	100mA	4
15	2.50	137	0.86	0.03	100mA	4
20	2.50	245	**-1.23**	0.21	100mA	4
30	2.50	562	1.18	0.67	100mA	4
40	2.50	1001	**-5.73**	0.37	100mA	4
40	7.50	323	-4.66	0.01	100mA	2
50	7.50	512	-26.8	0.71	50mA	4
60	7.50	742	-27.6	1.10	50mA	4
70	7.50	1014	-29.9	1.20	50mA	4
80	7.50	1329	-26.4	0.74	100mA	4
80	15.00	647	-14.9	0.04	100mA	2
90	15.00	825	-9.04	0.54	100mA	4
100	15.00	1024	-10.4	0.79	100mA	4

P4-1 (09^{0}30′57.80″; 006^{0}25′48.72″)
P4-5 (09^{0}31′10.76″; 006^{0}25′48.72″)
P4-9 (09^{0}31′23.72″; 006^{0}25′48.72″)

Along the Fifth North-South Profile (P5):
P5-2 (09^{0}31′01.04″; 006^{0}25′51.96″)

Along the Sixth North-South Profile (P6):
P6-2 (09^{0}31′01.04″; 006^{0}25′55.20″)
P6-3 (09^{0}31′04.28″; 006^{0}25′55.20″)
P6-11 (09^{0}31′30.18″; 006^{0}25′55.20″)
P6-16 (09^{0}31′46.38″; 006^{0}25′55.20″)

Along the Seventh North-South Profile (P7):
P7-16 (09^{0}31′14.00″; 006^{0}25′58.44″)

Along the Eight North-South Profile (P8):
P8-1 (09^{0}30′57.80″; 006^{0}26′01.68″)
P8-18 (09^{0}31′52.86″; 006^{0}26′01.68″)
P8-21 (09^{0}32′02.58″; 006^{0}26′01.68″)

Along the Ninth North-South Profile (P9):
P9-1 (09^{0}30′57.80″; 006^{0}26′04.92″)
P9-3 (09^{0}31′04.28″; 006^{0}26′04.92″)
P9-8 (09^{0}31′20.48″; 006^{0}26′04.92″)

Along the Tenth North-South Profile (P10):
P10-7 (09^{0}31′17.24″; 006^{0}26′08.16″)

Along the Twelfth North-South Profile (P12):
P12-8 (09^{0}31′20.48″; 006^{0}26′14.64″)
P12-11 (09^{0}31′30.18″; 006^{0}26′14.64″)

Along the Thirteenth North-South Profile (P13):
P13-8 (09^{0}31′20.48″; 006^{0}26′17.88″)
P13-10 (09^{0}31′26.96″; 006^{0}26′17.88″)

Along the Fourteenth North-South Profile (P14):
P14-8 (09^{0}31′20.48″; 006^{0}26′21.12″)
P14-9 (09^{0}31′23.72″; 006^{0}26′21.12″)

Along the Fifteenth North-South Profile (P15):
P15-3 (09^{0}31′04.28″; 006^{0}26′24.36″)
P15-4 (09^{0}31′07.52″; 006^{0}26′24.36″)

Along the Sixteenth North-South Profile (P16):
P16-7 (09^{0}31′17.24″; 006^{0}26′27.60″)
P16-12 (09^{0}31′33.42″; 006^{0}26′27.60″)

Along the Seventeenth North-South Profile (P17):
P17-6 (09^{0}31′14.00″; 006^{0}26′30.84″)
P17-8 (09^{0}31′20.48″; 006^{0}26′30.84″)
P17-11 (09^{0}31′30.18″; 006^{0}26′30.84″)
P17-12 (09^{0}31′33.42″; 006^{0}26′30.84″)
P17-13 (09^{0}31′36.66″; 006^{0}26′30.84″)
P17-14 (09^{0}31′39.90″; 006^{0}26′30.84″)
P17-15 (09^{0}31′43.14″; 006^{0}26′30.84″)

Along the Eighteenth North-South Profile (P18):
P18-7 (09^{0}31′17.24″; 006^{0}26′34.08″)
P18-8 (09^{0}31′20.48″; 006^{0}26′34.08″)
P18-9 (09^{0}31′23.72″; 006^{0}26′34.08″)
P18-12 (09^{0}31′33.42″; 006^{0}26′34.08″)

Along the Nineteenth North-South Profile (P19):
P19-7 (09^{0}31′17.24″; 006^{0}26′37.32″)
P19-8 (09^{0}31′20.48″; 006^{0}26′37.32″)
P19-9 (09^{0}31′23.72″; 006^{0}26′37.32″)
P19-12 (09^{0}31′33.42″; 006^{0}26′37.32″)
P19-15 (09^{0}31′43.14″; 006^{0}26′37.32″)

Along the Twentieth North-South Profile (P20):
P20-4 (09^{0}31′07.52″; 006^{0}26′40.56″)
P20-12 (09^{0}31′33.42″; 006^{0}26′40.56″)

Along the Twenty-first North-South Profile (P21):
P21-4 (09^{0}31′07.52″; 006^{0}26′43.80″)
P21-9 (09^{0}31′23.72″; 006^{0}26′43.80″)
P21-13 (09^{0}31′36.66″; 006^{0}26′43.80″)

The pseudosection plots

The pseudosection plot of P1: A synclinal high-resistivity material of fractured basement character is observed to have its low-resistivity trough centred on P1-10, P1-11, and P1-12 with its “minimum” obviously on P1-11; P1-11 has the lowest resistivity trend traceable from the surface to the maximum depth of *circa* 20 m-plus of all the survey points of P1. This pattern is discernible on the iso-resistivity plots and it is especially obvious at the 20 m-depth, the 40 m-depth, the 60 m-depth, the 70 m-depth, and the 90 m-depth designations. It would seem that the “locus” of the fractures discernible on the geoelectric cross-section of P1 at P1-5, P1-6, P1-7, and P1-13 is the resistivity “minimum” at P1-11.

The pseudosection plot of P2: The “minimum” of the synclinal high-resistivity material of fractured basement character along this second north-south profile is centred on P2-12; the lowest resistivity trend traceable from the surface to the maximum depth of *circa* 40 m-plus is between P2-11 and P2-12. It should be pointed out here that P2-11 lies exactly 100 m to the east of P1-11 along a straight line course and P2-12 is exactly 100 m to the north of P1-11 along a straight line course also; the line connecting P1-11 to P2-12 would be the hypotenuse of a triangle as it were. The pattern of resistivity low centred on P2-11 and P2-12 is discernible on the iso-resistivity plots and it is especially obvious at the 10 m-depth, the 20 m-depth, the 40 m-depth, the 70 m-depth, the 90 m-depth, and the 100 m-depth designations. It would seem that the “locus” of the fractures discernible on the geoelectric cross-section of P2 at P2-1, P2-3, P2-10, P2-13, P2-16, and P2-21 is the resistivity “minima” at P2-11 and P2-12.

The pseudosection plot of P3: A synclinal high-resistivity material of fractured basement character is observed to have its low-resistivity trough centred on P3-3 and P3-12; a low-resistivity "plunge" at depth is also observed at P3-1. Although the lowest resistivity trend traceable from the surface to the maximum depth of *circa* 60 m is centred on P3-3, this least resistivity trend can also be traced on P3-12 to a depth of *circa* 40 m-plus. P3-12 lies exactly 100 m to the east of P2-12 along a straight line course. The pattern of resistivity low centred on P3-12 is discernible on the iso-resistivity plots and it is especially obvious at the 1 m-depth, 10 m-depth, the 20 m-depth, the 40 m-depth, the 70 m-depth, the 90 m-depth, and the 100 m-depth designations; the pattern of resistivity low centred on P3-3 is discernible on the iso-resistivity plots and it is especially obvious at the 50 m-depth, the 70 m-depth, the 80 m-depth, the 90 m-depth, and the 100 m-depth designations. For P3-1, this pattern is obvious at the 80 m-depth, the 90 m-depth, and the 100 m-depth designations. The fractures discernible on the geoelectric cross-section of P3 at P3-1 and P3-3 exactly coincide with those of P3-1 and P3-3 of the pseudosection plot.

The pseudosection plot of P4: A deep-seated fracture structure is observed at P4-5, P4-9, and a synclinal high-resistivity material of fractured basement character is observed to have its low-resistivity trough centred on P4-2 and between P4-12 and P4-13; the lowest resistivity trend is traceable from the surface to the maximum depth of *circa* 20 m-plus at P4-2, P4-5, P4-12, and P4-13. The observation at P4-6 is being downplayed here because no data was collected at station P4-6 as a result of the "wet stream and thicket barrier." The pattern of resistivity low is centred on P4-2, P4-5, P4-9, P4-12, and P4-13 at the 70 m-depth, the 90 m-depth, and the 100 m-depth designations.

The pseudosection plot of P5: At P5-18, the low-resistivity trough of the synclinal high-resistivity material of fractured basement character corresponds to a very low-resistivity intrusion at the *circa* 70 m-depth mark. Other low-resistivity intrusions occur at P5-1, P5-5, P5-9, P5-10, P5-11, and P5-13; the lowest resistivity trend is traceable from the surface to the maximum depth of *circa* 50 m-plus at P5-5 and this trend is also traceable at the 20 m-depth mark at P5-9, P5-10, P5-11, P5-13, and P5-18.

The pseudosection plot of P6: Low-resistivity intrusions occur at P6-1, P6-5, P6-10, and P6-14; the low-resistivity trough of the synclinal high-resistivity material of fractured basement character that corresponds to a very low-resistivity intrusion at the *circa* 70 m-depth mark is seen at P6-18. The lowest resistivity trend is traceable from the surface to the maximum depth of *circa* 50 m-plus at P6-5 and this trend is also traceable at the 20 m-depth mark at P6-10, P6-14, and P6-18.

The pseudosection plot of P7: At P7-1 is a low-resistivity material at depth; this low-resistivity material at depth is a discernible trough of the synclinal high-resistivity material of fractured basement character at P7-5, P7-6, P7-7, P7-8, P7-14, P7-17, and P7-20. The lowest resistivity trend is traceable from the surface to the maximum depth of *circa* 20 m-plus at P7-1 and P7-7.

The pseudosection plot of P8: A low-resistivity occurrence at depth is what can be made out at P8-1 but this is now discernible as the trough of the synclinal high-resistivity material of fractured basement character at P8-3, P8-5, P8-7, P8-16, and P8-20. The lowest resistivity trend is traceable from the surface to the maximum depth of *circa* 20 m-plus at P8-1; P8-3, P8-7, and P8-20 are also identified by this material at the *circa* 10 m-depth mark.

The pseudosection plot of P9: A synclinal structure of comparatively high-resistivity is observed to have its low-resistivity trough centred on P9-7, P9-11, and P9-13; at the 60 m-depth mark of P9-1, a very low-resistivity structural emplacement can be made out upon keen observation. The lowest resistivity trend is traceable from the surface to the maximum depth of *circa* 70 m at P9-7 and this material is also seen at P9-11 and P9-13 at the *circa* 10 m-depth mark.

The pseudosection plot of P10: A synclinal structure of comparatively high-resistivity is observed to have its low-resistivity trough centred on P10-6; it is observed, too, that a tiny pocket of this material that corresponds to the low-resistivity trough is located at the 60 m-depth at P10-4. The lowest resistivity trend is traceable from the surface to the maximum depth of *circa* 15 m-plus at P10-6; P10-3 is flagged, too.

The pseudosection plot of P12: A synclinal structure of comparatively high-resistivity is observed to have its low-resistivity trough centred on P12-9; the lowest resistivity trend is traceable from the surface to the maximum depth of *circa* 15 m at P12-9.

The pseudosection plot of P13: A synclinal structure of comparatively high-resistivity is observed to have its low-resistivity trough centred on P13-10; the lowest resistivity trend is traceable from the surface to a depth of *circa* 10 m at P13-10.

The pseudosection plot of P14: A synclinal structure of comparatively high-resistivity is observed to have its low-resistivity trough centred on P14-8 and P14-10; observed at P14-5 is a vestige of a similar structure. The lowest resistivity trend is traceable from the surface to the maximum depth of *circa* 20 m at P14-10 and this material can also be identified at the near-surface of P14-8 and at *circa* 10 m-plus depth mark at P14-5.

The pseudosection plot of P15: At P15-2, there is a tiny pocket of very low-resistivity material located at the 50 m-depth mark that is enclosed within a comparatively high-resistivity material and a synclinal structure of comparatively high-resistivity is observed to have its low-resistivity trough centred on P15-5, P15-8, P15-11, and P15-13. The lowest resistivity trend is traceable from the surface to the maximum depth of *circa* 10 m-plus at P15-5, P15-8, P15-11, and P15-13; at P15-2, this material is seen at the very near-surface depth profile.

The pseudosection plot of P16: A synclinal structure of comparatively high-resistivity is observed to have its low-resistivity trough centred on P16-3, P16-6, and P16-13. The lowest resistivity trend is traceable from the surface to the maximum depth of *circa* 20 m-plus at P16-6; this material is seen at P16-3 at the *circa* 10 m-plus depth mark.

The pseudosection plot of P17: A synclinal high-resistivity material of fractured basement character is observed to have its low-resistivity trough centred on P17-3, P17-9, and P17-12. The lowest resistivity trend is traceable from the surface to the maximum depth of *circa* 30 m-plus at P17-3; this material is seen at P17-9 at the *circa* 20 m-plus depth mark. The fracture discernible on the geoelectric cross-section of P17 at P17-12 exactly coincides with that of P17-12 of the pseudosection plot.

The pseudosection plot of P18: A synclinal structure of comparatively high-resistivity is observed to have its low-resistivity trough centred on P18-4, P18-8, P18-10, and P18-14. The lowest resistivity trend is traceable from the surface to the maximum depth of *circa* 20 m at P18-4; this material is seen at P18-14 at the *circa* 20 m depth mark. The fracture discernible on the geoelectric cross-section of P18 at P18-8 exactly coincides with that of P18-8 of the pseudosection plot.

The pseudosection plot of P19: A synclinal structure of comparatively high-resistivity is observed to have its low-resistivity trough centred on P19-7, P19-10, and P19-13. The lowest resistivity trend is traceable from the surface to the maximum depth of *circa* 10 m at P19-13. The fracture discernible on the geoelectric cross-section of P19 at P19-7 exactly coincides with that of P19-7 of the pseudosection plot.

The pseudosection plot of P20: A synclinal high-resistivity material of fractured basement character is observed to have its low-resistivity trough centred on P20-4 and P20-12 plus a deep-seated intrusion at P20-15. The lowest resistivity trend is traceable from the surface to the maximum depth of *circa* 20 m at P20-15. The fracture discernible on the geoelectric cross-section of P20 at P20-4, P20-12, and P20-15 exactly coincide with those of P20-4, P20-12, and P20-15 of the pseudosection plot.

The pseudosection plot of P21: A synclinal high-resistivity material of fractured basement character is observed to have its low-resistivity trough centred on P21-5, P21-11, and P21-13; this material of low-resistivity trough is embedded on P21-8 and it can also be traced on P21-3. The fracture discernible on the geoelectric cross-section of P21 at P21-8, P21-11, and P21-13 exactly coincide with those of P21-8, P21-11, and P21-13 of the pseudosection plot.

The Iso-resistivity maps at depths

The 1 m-depth map: This near-surface layer shows a widespread low-resistivity character (sub-200 Ωm) across the 4 km^2 area of study except at the central northeast region and a small flank at the southeast and especially the central southeast where progressively higher resistivities can be discerned.

The 10 m-depth map: The sub-200 Ωm character still predominates across the entirety of this 4 km^2 areal extent except at some scattered portions of the central to the north central regions and one small region of the central southeast where resistivity values greater than 750 Ωm can be discerned; this localized “high” can be traced in the preceding 1 m-depth map.

The 20 m-depth map: The entire central and southwest portions at this depth are characterized by that “widespread low-resistivity character (sub-200 Ωm)”. Progressively high-resistive materials are beginning to “show up” in the northwest and southeast flanks; that “*one* small region of the central southeast where resistivity values greater than 750 Ωm can be discerned” can also be traced on this map.

The 30 m-depth map: The northwest to the top central segment is characterized by clear showing of increasing resistivities (between 200 and 750 Ωm); the segment of the southwest that is characterized by this range has increased also, however, that “*one* small region of the central southeast where resistivity values greater than 750 Ωm can be discerned” can also be traced on this map.

The 40 m-depth map: A progressive spike in the values of resistivities can be made out overall across the different segments that have been identified in the preceding discussion. In the northwest, top northcentral, and the flanks of the southeast the “benchmark” of the low that corresponded to 200 Ωm in the preceding discussion now corresponds to the 400 to 500 Ωm across these different segments. Now, too, that “*one* small region of the central southeast where resistivity values greater than 750 Ωm can be discerned” has new high values between 1200 to 1600 Ωm.

The 50 m-depth map: At this depth, the materials that are

characterized by “progressive spike in the values of resistivity” seen in isolation at the “northwest, top northcentral, and the flanks of the southeast” have now formed one contiguous body with its overall values of resistivity between 300 to 800 Ωm; there are small points of resistivity highs (800 to 1400 Ωm) dispersed amongst this contiguous body, and interestingly too, sub-300 Ωm “pinchouts” are identified around the top north central region, just left of the top midplane section, the south east and along the true eastern flank close to the midplane section. The “*one* small region of the central southeast where resistivity values greater than 750 Ωm can be discerned” has now assumed a sub-750 Ωm character. At the “consistent-low” regions of the central to the southwest portion, an isolated body of high resistivity, seen as a mere blob in the 40 m-depth, is now assuming a prominent dimension in its isolation. Compared to the 40 m-depth map, resistivity values overall have dropped slightly here.

The 60 m-depth map: At this depth, the pattern at the 50 m-depth repeats here, even as to the distribution of the “pinchouts,” but overall layer resistivity values have gone slightly when compared to those of the 50 m-depth map; a very prominent “pinchout” can now be traced at the lower southeast portion.

The 70 m-depth map: At this depth, the “benchmark” of resistivity low is 600 Ωm which marks an overall increase of resistivity across all the segments of the 4 km^2 area of study under consideration here. This being the case, the central to the southwest portion is still characterised by comparatively low resistivity values (sub-600 Ωm); in this vein, too, a prominent “pinchout” can also be traced at the northwest and significant “pinchouts” can be traced at the central southeast and the true eastern flank close to the midplane section. Close to the prominent “pinchout” in the northwest is a localised region of very high resistivity that can be traced in the 60 m- and 50 m-depth maps.

The 80 m-depth map: At this depth, there is observed steadily increasing values of resistivity toward the southwest, as if pushing from the north and southeast; the “benchmark” of resistivity low is now 400 Ωm which marks an overall decrease of resistivity across all the segments of the 4 km^2 area of study under consideration here. The pattern of “pinchouts” is like those observed in the 70 m-depth map but the one observed at “*the true eastern flank close to the midplane section*” is now located above the midplane section along the true eastern flank.

The 90 m-depth map: At this depth, a “northern zone” of very high resistivity values can now be contrasted from a “southern zone” of comparatively low resistivity values. The pattern of pinchouts observed in the 70 m-depth map have all disappeared but a large isolated body of low-resistivity “pinchout” (sub-300 Ωm) is the prominent feature in the central to the southwest region. Overall, there is an overall decrease of resistivity across all the segments compared with those of the 80 m-depth map.

The 100 m-depth map: The pattern of resistivity values at the 90 m-depth map repeats here and the size of the ‘*large isolated body of low-resistivity “pinchout” (sub-300 Ωm)*’ has shrunk slightly; this means, too, that at this 100 m-depth “*there is an overall decrease of resistivity across all the segments compared with those of the 80m-depth map.*” This fact makes for an interesting conclusion indeed. At this 100 m-depth, the proportion of materials of resistivity highs (750 to 1450Ωm) has increased appreciably.

Fault-trace of water-bearing fracture signatures inferred from a combination of the geoelectric cross-sections and the induced polarisation tables on the satellite imagery map of the area of study with the developed phase I in the background

The fault-trace of water-bearing fracture signatures inferred from a combination of the geoelectric cross-sections and the induced polarisation tables on the satellite imagery map of the area of study with the developed Phase I in the background is represented in Figure 16.

In Figure 16, the diagonal fault-traces of fracture signatures are observed in perspective with respect to the location and areal extent of the developed portion of the Gidan Kwano Campus. It is observed that the broader southwest region of the western edge of the developed portion of the GKC is characterised by a concentration of subsurface water-bearing fractures that are apparently connected by diagonal fault-line traces.

Summary of the study

On the number of layers derivable from VES data processing by the WinResist® Software: The theoretical number of layers obtained across the VES stations where data was collected ranges from three to seven; a three-layer sequence of topsoil, weathered zone, and fresh basement is the unanimously-accepted subsurface layering defined for the wider area of which the area of study is but a part of. Multi-layer (up to six or seven layers) log-log plots were obtained for profile lines (P17 to P21) of the central southeast segment where outcrops profuse and subsurface resistivity are high in contrast to the southwest segment (P1 to P9) where outcrops are few and far between and subsurface resistivities are comparatively low; generally, four layers or less are observed at the southwest.

On the occurrence of consistently-low resistivity at depths: This situation occurs at the southwest segment

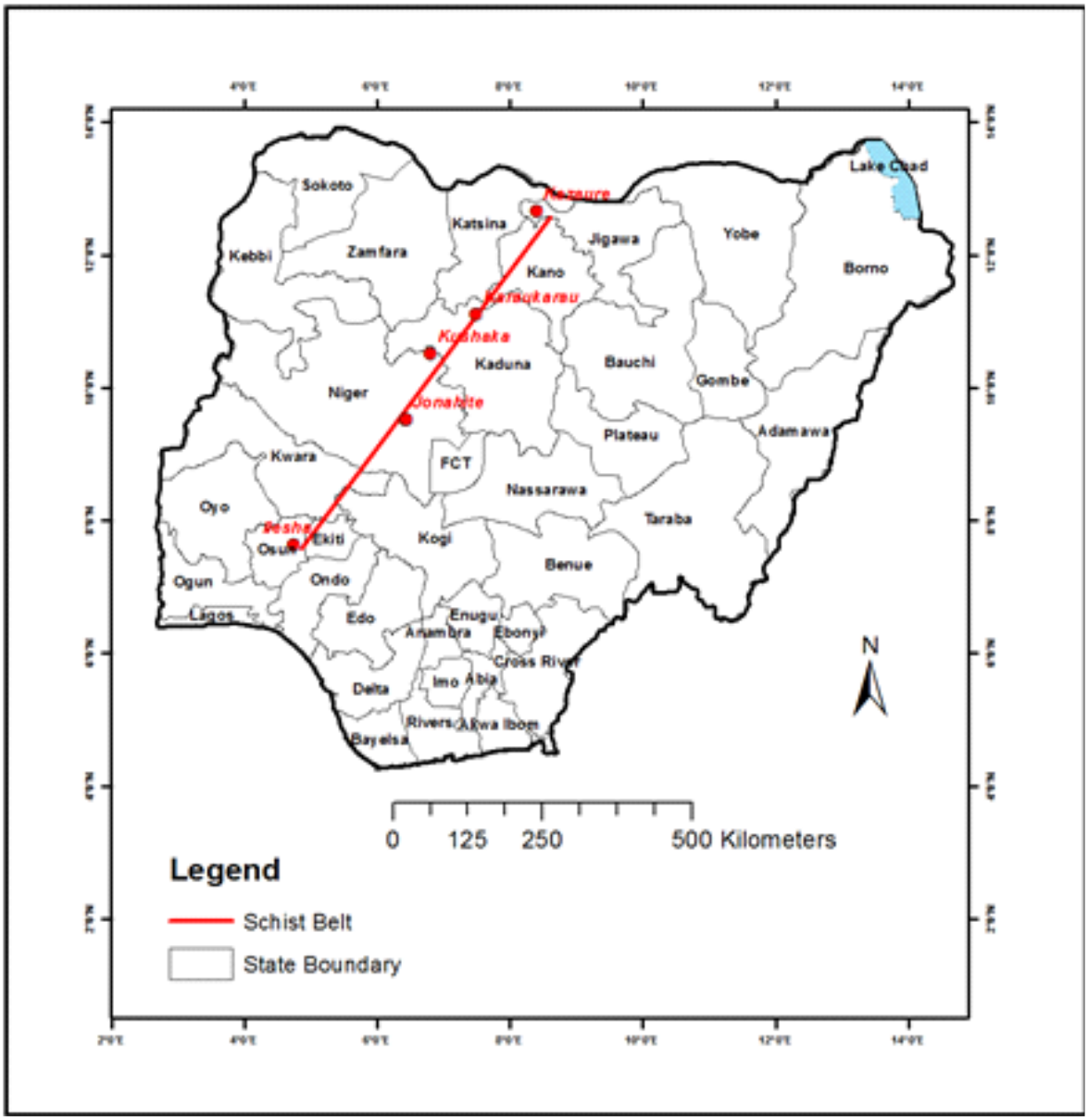

Figure 17. NE-SW fault-traces ("Jonahite") aligns exactly with the Kazaure-Karaukarau-Kushaka-Ilesha Schist Belt.

(P1 to P9, especially) where up to the 80 m-, 90 m-, 100 m-depths, a rather continuous intrusive body of low-resistivity zones appears to form jagged "sinks" (between P3-1 and P9-1) from "sources" in the mid-plane of the area of study.

On the occurrence of deeply-incised water-bearing fractures in the body of the fresh basement rock: Deeply-incised water-bearing fractures in the body of the fresh basement rock most commonly occur at the southwest segment (P1 to P9) where outcrops are few and far between and subsurface resistivity are comparatively low.

On the profusion of water-bearing fracture signatures: Overall, comparatively more water-bearing fracture signatures per profile line of the central southeast segment (P17 to P21) are noticed for each of P17, P18, P19, P20, and P21 than for corresponding profile lines at the southwest segment (P1, P2, P3, P4, and P5). Whilst the fractures at the southwest segment are deeply-incised, those at the southeast are comparatively shallow. Water-bearing fractures are plentiful in the central southeast segment, they are more closely-spaced but they are comparatively shallow; in the southwest segment they are more dispersed, but are deeply-incised in the local

basement rock of the area of study.

On the lengths of the southwest-trending fault-traces discernible in the subsurface: The lengths of the southwest-trending fault-traces terminating at point P2-1 is 1.3 km, the one terminating at P3-1 is 1.8 km, at P4-1 is 1.7 km, at P8-1 it is 1.4 km, and P9-1 it is 1.5 km, and at P6-2 it is 1.7 km.

On the benefits of IP table of values as quality control tools: The IP table of values assisted in the association of a fracture signature with groundwater accumulation or the lack of groundwater thereof; in reality, for this study, the IP table of values was a quality control "eliminator." This IP "eliminator" QC process was especially invoked when analysing the fracture signatures observed in the geoelectric section of P6; fracture signatures were identified at P6-2 at the 73 m depth-mark, at P6-3 at the 26 m depth-mark, at P6-11 at the 37 m depth-mark, at P6-13 at the 6 m depth-mark, at P6-16 at the 84 m depth-mark, at P6-19 at the 100 m depth-mark, and at P6-20 at the 100 m depth-mark. As a result of the IP "eliminator" QC process, the fractures identified at P6-13, P6-19, and P6-20 were eliminated as water-bearing fractures. In this vein, P10-1, P20-15, P21-8, P21-11, and P21-12 were also eliminated as water-bearing fractures or as "fractures of interest."

On the vestige of a regional geological structure: The fault-traces decipherable in Figure 16 are oriented in a northeast-southwest (NE-SW) sense. Jonah and Adebayo (2019) have shown that there exists a comparatively significant count of weathered schist outcrops along this NE-SW diagonal on the plane of the 4 km^2 study area. A twist of serendipity ensures that these subsurface NE-SW fault-traces, flagged for their groundwater and mineralization prospects, and discerned at the east-central portion of the Gidan Kwano Campus in a diagonal across the 4 km^2 core study area, aligns exactly with the Kazaure-Karaukarau-Kushaka-Ilesha Schist Belt. In the modern geography setting of the present time, the Kazaure-Karaukarau-Kushaka-Ilesha Schist Belt actually traverses a lengthy diagonal across the landscape of Nigeria, cutting through such Nigerian states as Jigawa, Kano, Kaduna, Niger, Kwara, Ekiti, and Osun. In order to ensure ease of reference to the comparatively tiny segment of the vestige of the Kazaure-Karaukarau-Kushaka-Ilesha Schist Belt through the 4 km^2 core study area represented as the discerned fault-traces of Figure 16, a rather light-hearted nomenclature scheme of "Jonahite" was assigned to this vestige of that prominent schist belt through the 4 km^2 plane seen in Figure 16. Please see Figure 17 also.

It is understood from Obaje (2009) that the quartet of the schist belts mapped in Nigeria has the common denominators of trend (the NE-SW orientation) and geographic attribute (occurrence mapped west of 8^0 longitude). It was also gathered that the schist belts of Nigeria are associated with gold mineralisation. Actually, there is a rich body of work at the wider 8 km^2 that progressively gives indication about the significant groundwater character and possible mineralisation of the discerned fault-trace diagonals and these are cited as follows: Jonah et al. (2015a), Jonah et al. (2015b), Jonah et al. (2015c), Jonah and Olasehinde (2015), Jonah et al. (2015d), Jonah and Jimoh (2016), Jonah and Saidu (2016), Jonah (2016), Jonah and Adamu (2017), Jonah and Abdulrasheed (2018), and Jonah and Ibrahim (2018).

CONFLICT OF INTEREST

The authors declare that they have no conflict of interest.

REFERENCES

Acworth, R. I. (1981). *The evaluation of groundwater resources in the crystalline basement of northern Nigeria*, PhD Thesis, University of Birmingham.

Adesoye, S. A. (1986). *Master plan of the Federal University of Technology's permanent site, Minna*. Adesoye and Partners, Kaduna, Nigeria.

Akca, I. (2016). ELRIS2D: A MATLAB package for the 2D inversion of DC resistivity/IP data. *Acta Geophysica*, 64(2), 443-462.

Coggon, J. H. (1971). Electromagnetic and electrical modeling by the finite element method. *Geophysics,* 36(1), 132-155.

Dey, A., & Morrison, H. F. (1979a). Resistivity modelling for arbitrary shaped two-dimensional structures. *Geophysical Prospecting*, 27, 1020-1036.

Dey, A., & Morrison, H. F. (1979b). Resistivity modeling for arbitrarily shaped three-dimensional shaped structures. *Geophysics*, 44, 753-780.

Jonah, S. A. & Abdulrasheed, S. A. (2018). Analysis of self-potential data at a 0.6 km^2 swath of the southern Phase II Development, Gidan Kwano Campus, Minna, northcentral Nigeria. *International Journal of Industrial Technology, Engineering, Science, and Education,* 1(2), 42-49.

Jonah, S. A. (2016). Analyses of pseudosection specific routes of different orientations of fault-traces to determine groundwater flow pattern at a 4 km^2 tranche of New Development, Gidan Kwano Campus Phase II, Federal University of Technology, Minna, Nigeria. *Journal of Science, Technology, Mathematics, and Education,*12(3), 9-18.

Jonah, S. A., & Adamu, I. B. (2017). Extraction of depth-to-basement information from the interpretation of vertical electrical sounding data of Gidan Kwano Campus Phase II, Federal University of Technology, Minna, Nigeria. *Journal of Information, Education, Science, and Technology,* 4(1), 126-132.

Jonah, S. A., & Adebayo, H. M. (2019). *Macroscopic petrographic control of a 4 km^2 VES study at the southern phase ii development, Gidan Kwano Campus, Minna, Nigeria*, BTech Thesis, Federal University of Technology, Minna.

Jonah, S. A., & Adegboye, J. A. (2019). *Investigating lateral variations of resistivity of a 4 km^2 VES study at the southern phase ii development, Gidan Kwano Campus, Minna, Nigeria*, BTech Thesis, Federal University of Technology, Minna, Nigeria.

Jonah, S. A., & Ibrahim, M. (2018). *Investigation of patterns of self-potential manifestations across the southernmost 0.4 km^2*

tranche of the phase ii development, Gidan Kwano Campus, Minna, Northcentral Nigeria, BTech Thesis, Federal University of Technology, Minna.

Jonah, S. A., & Jimoh, M. O. (2016). Validity of an empirical rule for delineating aquifer prospects at the Gidan Kwano Campus Development Phase II, Federal University of Technology, Minna, Northcentral Nigeria. *Journal of Science, Technology, Mathematics, and Education,* 12(2), 18-24.

Jonah, S. A., & Olasehinde, P. I. (2015). Qualitative induced polarisation validation of the results of a 2 km^2 VES study completed at the Gidan Kwano Campus Phase II Development, Federal University of Technology, Minna, Nigeria. *Journal of Science, Technology, Mathematics, and Education,* 11(3), 34-46.

Jonah, S. A., & Saidu, S. (2016). On the correlation of area of consistently-low resistivity at depths with slope of the landform of a 4km^2 tranche of the Gidan Kwano Campus Development Phase II, Federal University of Technology, Minna, Northcentral Nigeria. *Journal of Science, Technology, Mathematics, and Education,*12(2), 34-39.

Jonah, S. A., Akpomie, D. P., Ezekwebekwe, L. O., Isah, E.A., Muhammed, A.N., Momoh, A.A., Okoye, C.K., Okpara, K. K., Oni, N.O., Alade, R. O., Yahaya, G. A., Zubair, R. O., Onoja, E. U., & Daramola, O. (2015a). A dual topographic-petrographic control for a 1 km^2 VES-IP study completed at the Gidan Kwano Campus Phase II Development, Federal University of Technology, Minna, Nigeria. *Journal of Information, Education, Science, and Technology,* 11(3), 65-76.

Jonah, S. A., James, G. O., Adeku, D. E., Ahmed, F., Alhassan, A., Hamza, S., Igbideba, O. I., Kyari, M., Kwaghhua, F. I., Macaulay, V. F., Olarewaju, S. I., Onyeodili, G., Popoola, G.B., Sofeso, O.A., Switzer, F. K., & Umoh, U. E. (2015b). Geoelectrical investigation for aquifer and geotechnical properties at the planned Gidan Kwano Campus Development Phase II, Federal University of Technology, Minna Minna, Nigeria. *Journal of Science, Technology, Mathematics, and Education*, 11(2), 81-100.

Jonah, S. A., Olasehinde, P. I., & Umar, M. (2015^c). Evaluation of geomorphological quality control of geo-electrical data at Gidan Kwano Campus, Federal University of Technology, Minna, Central Nigeria. *Journal of Information, Education, Science, and Technology*, 2(1), 122-134.

Jonah, S. A., Olasehinde, P. I., Jimoh, M. O., Umar, M., & Yunana, T. (2015d). An intercalated dual geoelectrical survey of an earlier study for groundwater at the planned Gidan Kwano Campus Development Phase II, Federal University of Technology, Minna, Nigeria. *Journal of Information, Education, Science, and Technology,* 11(2), 32-50.

Koefoed, O. (1979). *Geosounding Principles 1: Resistivity Sounding Measurements*, Elsevier Science Publishing Company, Amsterdam.

Loke, M. H. (2001). *Tutorial: 2-D and 3-D Electrical Imaging Surveys*, Google search, 8thAugust 2018, 11:08 a.m.

Mufti, I. R. (1976). Finite-difference resistivity modeling for arbitrarily shaped two-dimensional structures. *Geophysics,* 41(1), 62-78.

Obaje, N. G. (2009). *Geology and Mineral Resources of Nigeria*. In: Lecture Notes in Earth Sciences, Springer-Verlag, Berlin.

Pelton, W. H., Rijo, L., & Swift, C. M. (1978). Inversion of two-dimensional resistivity and induced-polarisation data. *Geophysics,* 43 (4), 788-803.

Rijo, L. (1977). *Modeling of Electric and Electromagnetic Data*, PhD Thesis, University of Utah Salt Lake City, USA.

Salako, K. A., & Udensi, E. E. (2005). Vertical electrical sounding investigation of the western part of the Federal University of Technology, Minna. *Proc: First Annual School of Science Education Conference (Federal University of Technology, Minna)*, 1, 69-78.

Udensi, E. E., Unuevho, C. I., Jonah, S.A., Ofor, P. N., Adetona, A. A., Salako, K. A., Gana, C. S., Nwosu, J. E., Mulero, E. O., Iwuafor, H. O., Akinloye, O. A., & Owolabi, E. O. (2006). Geoelectrical survey for groundwater at the Gidan Kwano Campus of the Federal University of Technology, Minna. *Environmental Technology and Science Journal,* 1(1), 16-48.